International Journal of Advances in Scientific Research and Engineering (ijasre)

E-ISSN : 2454-8006

DOI: 10.31695/IJASRE.2025.4.2

Volume 11, Issue 4
April - 2025

The Relation Study between Geochemical and Geomechanical Properties of Shale Formation: A comprehensive review

Tantine Vita Makiese[1], & **Zanga Landu Christian**[2]

[1*] Faculty of Oil, Gas and Renewable Energies

Department of Exploration and Production, University of Kinshasa

D.R. Congo.

[2]School of Environment, Department of Environmental Science,

China University Of Geosciences, China

ABSTRACT

Understanding the effects of geochemistry and mineral composition on geomechanical characteristics is critical in the design and optimization of hydraulic fracturing necessary for shale gas reservoir production. Fundamental information is still missing in experimental methodologies used to evaluate the influence of geochemical parameters and mineral composition on geomechanical properties of shale gas reserves. This paper provided an in-depth assessment of the various experimental methodologies and their applications in the relationship between the geomechanical and geochemical features of the Longmaxi shale formation. The limits of these methodologies were recognized, comparative analyses on experimental data and geomechanical parameters were performed, and recommendations for improved geomechanical assessments were provided. This review will contribute to fundamental understanding and will guide future experimentally-based geochemical and geomechanical investigations on shale gas reserves.

Keywords: Geomechanical properties, Geochemical evaluations, Mineral composition, Shale gas formation.

I. INTRODUCTION

Exploration and exploitation of unconventional oil and gas resources are essential given the growing demand for clean energy on a worldwide scale. Potentially among the most significant unconventional resources is shale. The boom in unconventional shale plays has increased interest in shale rocks over the past 10 years, and their exploration and development have now taken center stage in the world's oil and gas exploration. These prospective energies and decarbonization systems contain significant amounts of shale, a word used here to refer to fine-grained sedimentary rocks with varied mineralogy. Due to their low matrix permeability and high capillary entry pressure, they serve as subsurface seals and act as reservoirs for the production of unconventional gas. Controlling the flow and potential leakage of fluids is essential to achieving long-term (>10,000 yr) geological storage goals.

Due to the complicated nature of fluid storage, shale reservoirs are more difficult to discover, quantify, and exploit than conventional reservoirs. Total organic carbon content (TOC), thermal maturity, fluid content, and reservoir lithologic quality data (mineral composition, porosity, permeability, and thickness) have been identified as some crucial parameters for evaluating reservoir properties by studies carried out in China [1, 2]. The composition, porosity, and water content of the shale, as well as the pressure (P) and temperature (T) conditions, although not as much as the strain rate, have a significant impact on the geomechanical parameters such as compressive strength and elastic moduli. Shale rocks are made up of mineral particles.

The mineral makeup of a single reservoir in various local zones can vary significantly, which has an impact on the geomechanical and petrophysical characteristics of shale. It has been discovered that the reservoir has the greatest potential for gas and oil production due to optimal reservoir conditions. The essential metrics (thermal maturity, total organic carbon, porosity, and mineral composition) are used to assess the reservoir attributes. The main elements influencing the enrichment and high production of shale gas resources are known to have a high total organic carbon (TOC) content, high brittleness, high formation pressure, and structural preservation requirements. It is crucial to recognize and comprehend the parameters influencing a shale reservoir's geomechanical properties since these features are crucial for both the emergence of spontaneous fractures and the formation's reaction to hydraulic fracture stimulation. In order for shale gas to migrate from the shale matrix to the wellbore locations, broad and dense fracture networks must be created during hydraulic fracturing operations [3]. Basic geomechanical and petrophysical characteristics are crucial for hydraulic fracturing design and optimization, especially in reservoir conditions. According to earlier studies [4], geomechanical characteristics play a crucial role in the onset, propagation, and closure of fractures.

Shale's elastic qualities are one of the most crucial factors to understand for hydraulic fracturing success, which is required for production from unconventional reservoirs with a lot of organic material. As multiphase and multiscale material systems with inherent heterogeneity in chemical composition [including organic diversity (particularly maturity) and mineralogy], microtexture, and mechanical qualities [5], geomaterials like organic-rich shales can be regarded as such [6]. As a result, shales' elastic characteristics, which have an impact on both fracturing methods and the flow of hydrocarbons into the wellbore, received a lot of attention. In recent years, numerous studies have been conducted to characterize and quantify elastic parameters (Young's modulus and Hardness) on the bulk, micro, and nano-scale mechanical properties of significant shale plays in the US and around the world [7-10].

However, without significantly changing the mineralogy, elements like texture and diagenesis can still have an impact on mechanical performance [11]. Determining and capturing the governing mechanical processes in an adequate upscaling model is consequently extremely difficult. By spreading uncertainty through a multiscale homogenization model utilizing a probabilistic methodology, recent studies have started to account for the underlying heterogeneity of the shale reaction [12]. In this context, standard bulk geomechanical testing, a common method to determine elastic characteristics, is costly, time-consuming, and impractical because access to core samples is limited [13]. Shale reservoirs also have a very difficult time making larger samples available and ready. As a result, in recent years [9, 14, 15], researchers have started to explore the mechanical properties of shale at the micro- and nanoscale.

Many geomechanical testing methods, including the unconfined and triaxial compression tests, are based on force-displacement (F-D) mechanisms. To examine the mechanical properties of various earth materials, sophisticated characterization techniques have significantly increased the F-D resolution of measurements. Similarly, nanoindentation, which is extensively used in material characterization, offers a direct assessment of elastic characteristics at the nanoscale.

In order to improve the assessment of the effects of geochemical characteristics and mineral compositions on the geomechanical properties of the Longmaxi shale formation, comparative analyses of experimentally derived geomechanical parameters, geochemical characteristics, and mineral compositions of the Longmaxi shale formation were conducted. This review will broaden our understanding of the relationships between geochemical and geomechanical characteristics of shale gas reservoirs and their effects on geomechanical parameters of the Longmaxi shale formation. It will also serve as a guide for future experimental research on these relationships.

DOI: 10.31695/IJASRE.2025.4.2

2. THE LAW OF GEOCHEMICAL REACTION PROPERTIES CHANGES IN THE BURIAL EVOLUTION HISTORY

Following a number of tests, scientists have discovered that three crucial factors organic matter richness, thermal maturity, and kerogen types—are necessary for an appropriate evaluation of hydrocarbon-forming circumstances. According to [16], a source rock's total organic carbon (TOC) consists of three main components: organic carbon in retained hydrocarbons, organic carbon that can be converted to hydrocarbons (also known as convertible, reactive, or labile carbon), and carbonaceous residue that won't produce hydrocarbons due to a lack of hydrogen, also known as inert, dead, or residual organic carbon [17]. The extremely developed Longmaxi marine shale, according to Boning Zhang et al. (2020), is one of the most important options for the commercial exploitation of shale gas resources in China [18]. The basal section of the Longmaxi Fm generally has the largest organic matter concentration. TOC content varies with lithofacies, with siliceous and carbonaceous shale having the highest TOC levels. TOC concentration varies with lithology, with siliceous shales and clay shales having the greatest levels. The high TOC concentration diminishes higher in the Lower Longmaxi shale. As the sand content increases, the organic matter content eventually declines.

Wang Ruyue et al. (2019) discovered that the TOC content, organic matter type, and age of the Wufeng-Longmaxi shale vary little across the Sichuan Basin and its perimeter [19]. Based on carbon isotope composition, organic petrology, and organic geochemistry of kerogen, organic materials are mostly kerogen types I and II, with lower plankton serving as the primary source of hydrocarbon production material [20]. Despite the fact that the Wufeng-Longmaxi shales in the Sichuan Basin and its perimeter are relatively varied, the value of equivalent vitrinite reflectance (Ro) is concentrated in the 2.3%-3.1% range, indicating an over-mature state. Furthermore, there is no association between shale thermal maturity and present burial depth, indicating that there is no risk of exceedingly high thermal maturity. Furthermore, only the Xuanhan-Shizhu area in the northeastern Sichuan Basin and the Yibin-Luzhou area in the southern Sichuan Basin have higher thermal maturity values and Ro values larger than 2.8%. also, Shugen Liu et al. (2013) demonstrated that total organic carbon in the Longmaxi Formation shale is very varied through analyses of field samples and core samples from petroleum exploration wells [21]. The TOC of the black shale near the formation's base ranges from 0.35% to 6.7%, with an average of 1.5%. The TOC in the upper Longmaxi Formation is substantially lower, ranging from 0.08% to 0.8%.

2.1. Organic matter and kerogen type

Chao Liang et al. (2014) used petrographic studies and maceral analyses to discover that the Longmaxi shale contains a lot of sapropelinite (mostly asphaltene) and a little bit of inertinite and liptinite, but no vitrinite [22]. The organic matter type was identified by kerogen element analysis (H/C and O/C). The atomic H/C vs O/C ratio is frequently used to distinguish between kerogen kinds. This figure demonstrates that the kerogen is mostly Type I (Fig. 1a). They also demonstrated that the Longmaxi shale has a maximum TOC level of 4.79 wt.% and an average of 2.76 wt.%. Because higher terrestrial plants had not emerged by the Silurian, plankton dominates organic material in the shale. This may help to explain why type I oil-prone kerogen dominates organic materials. Because organic shale samples in the Longmaxi Formation exhibit extraordinarily high Tmax values and low HI values, the Van Krevelen diagram is ineffective for distinguishing organic matter types [23, 24]. As a result, they employ kerogen microcomponents and isotopes to detect the kind of organic materials.

DOI: 10.31695/IJASRE.2025.4.2

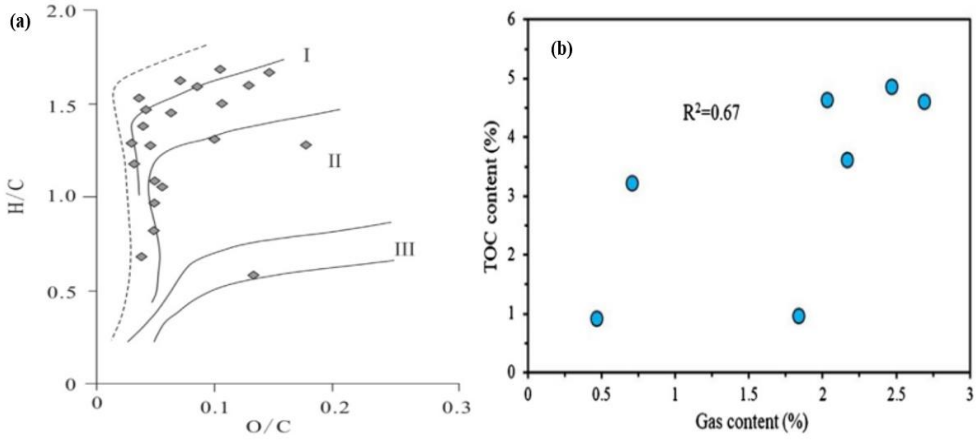

Fig.1: (a). The organic matter types of the Longmaxi shale. [22]; (b). Cross plot of TOC content versus gas content of the Longmaxi shale in northern Guizhou area. [25]

In addition, Shangbin Chen et al. (2014) investigated on samples from the bottom section of the Longmaxi Formation to better understand the fluctuation of geochemical characteristics of shale throughout burial development [26]. The thickness of the black shale was discovered to be between 10 and 170 m. The Changning-Naxi-Yongchuan area has the thickest reservoir. The TOC of the shale near the formation's bottom (50-m thickness) is greater than 2.0%. TOC lateral distribution varies with thickness lateral distribution, with greatest TOC in the Gongxian-Luzhou-Yongchuan area. The burial depth varies between 2000 and 4500 meters. The shale has reached thermal maturity. The examination of reservoir features reveals that the Longmaxi Formation in China's southern Sichuan Basin possesses circumstances favorable for shale gas formation and consequently resource potential. Also, Yi zhong et al. (2021) investigated the chemical and isotopic compositions of seven gas samples from the Longmaxi shale [25]. The results indicated that this shale gas is thermogenic in origin and oil-derived, as shown in Fig.1b, and that the over-mature evolution (2.18-3.12%) resulted in the reversal of carbon isotopic compositions. The organic materials in the shale samples are mature, with Ro ranging from 2.18 to 3.12%, showing that the organic matters developed into a dry gas window. Visual examination of the organic matter indicates that the kerogen type index (TI) ranges between 47 to 57, indicating that these organic materials are humic-sapropelic. The TOC levels of these shale samples range from 0.92-4.87%, with an average of 3.26%. Except for samples S1 and S2, all of the shale samples in this investigation had TOC values of at least 3.22%. In this investigation, the gas contents of shale samples ranged from 0.47 to 2.69 m3/t, with an average of 1.76 m^3/t, and the gas contents were positively connected with TOC levels, with a correlation value of 0.67. Boning Zhang et al (2020) examined the frequency distribution of TOC concentration in the Longmaxi Formation using a CS230 carbon/sulfur analyzer (LECO, St. Joseph, USA) and samples crushed into powder smaller than 100-mesh [18]. The findings of measuring the TOC content in 122 samples indicated that the TOC concentration ranged from 0.43% to 8.39%, with an average value of 2.20% in the Longmaxi Formation of the Sichuan Basin. 57.38% of samples have a TOC content less than 2.00%, whereas 42.62% have a TOC content greater than 2.00%. This indicates the abundance of TOC in the Longmaxi Formation, which is beneficial for shale gas generation and storage (Fig.2).

DOI: 10.31695/IJASRE.2025.4.2

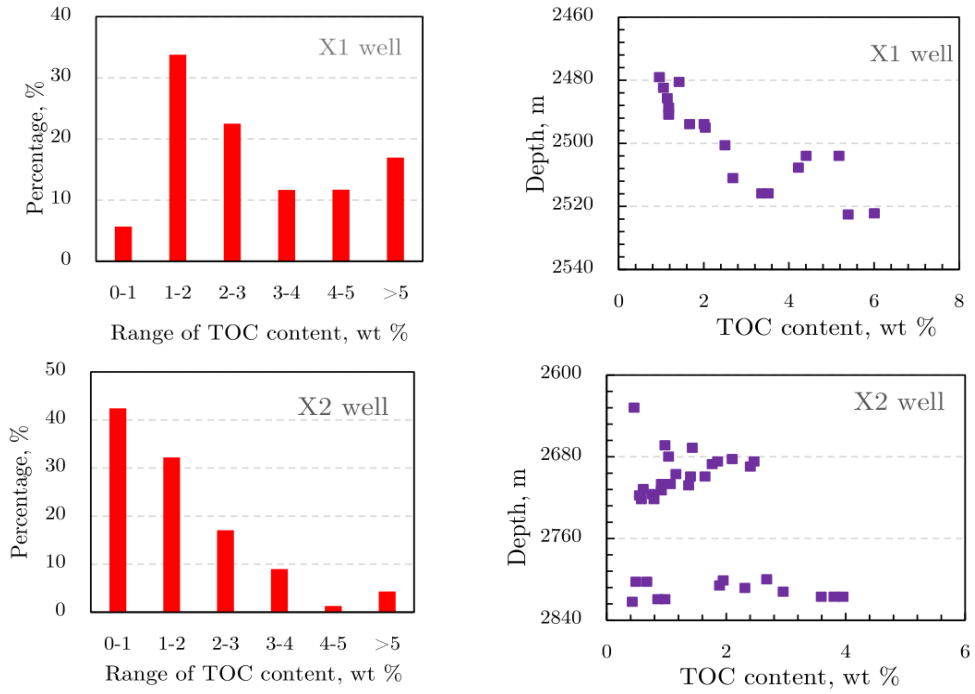

Figure 2. The frequency distribution histogram of TOC content as well as its relationship with depth in the Longmaxi Formation. [18]

2.2. Thermal maturity

Thermal maturity, assessed using a vitrinite reflectance approach, is an important characteristic for determining the maturity of rocks [27]. To assess the age of the shale formations, the Ro% was utilized as a quantifiable measure. According to Hunt (1996), considerable amounts of gas may be created principally through secondary cracking of in situ oils in thermally mature locations [28]. As a result of its higher thermal maturity, the Longmaxi Formation has the greatest potential for gas production. Tuzingila R.M. et al. (2024) discovered that the Longmaxi shale is in a very developed stage, with comparable vitrinite reflectance ranging from 1.6% to 2.28%, with an average of 2.05% [5]. The Ro value indicates that the source rock has passed through the thermal gas window. According to Shangbin Chen et al. (2014), the vitrinite reflectance values (after conversion to comparable marine facies vitrinite reflectance) vary from 1.84% to 3.30%, with a mean value of 2.69% [26]. According to the vitrinite reflectance values (Ro > 2.0%), it is excessively mature [29]. The thermal maturity indicates that the Longmaxi Formation is in the (dry) gas production window in the studied region. The source rock produces mostly dry gas (methane) and a little quantity of gas condensate during the over-mature thermal stage [30]. Additionally, Guang Hu et al. (2020) used organic petrology, focused ion beam-environmental scanning electron microscopy (FIB-SEM), and low-pressure N^2 adsorption and desorption to analyze six shale samples that were taken from the Shuanghe section and wells YS118 and JY2 in the Sichuan Basin [31]. They found that the mean Requ of sample YS-01 from well YS118 is 2.70% with a standard deviation of 0.21 (n = 66, R_{equ} ranges from 2.25% to 3.72%), and the mean R_{equ} of sample JY-01 is 2.48% with a standard deviation of 2.33 (n = 65, R_{equ} ranges from 1.91% to 3.36%) (Fig. 3).

DOI: 10.31695/IJASRE.2025.4.2

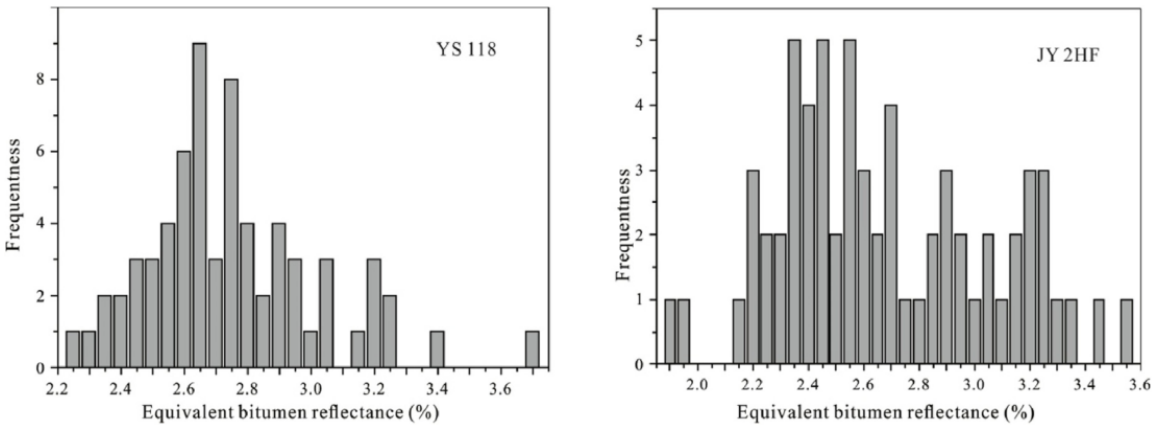

Fig.3. Histograms of bitumen reflectance values of the Longmaxi shales from wells YS 118 and JY 2HF. [31]

3. THE LAW OF GEOMECHANICAL PROPERTIES

Shale gas reservoirs, also known as source rock reservoirs (SRR), have several unique characteristics that make hydraulic fracturing an important choice for starting an economic level of natural gas production. In contrast to typical gas reservoirs, the poor permeability, ultra-low porosity of shale rock, and restricted reservoir contact area of this enormously organic-rich deposit do not allow for economic production without stimulation operations. Many research are carried out, ranging from shale pore-scale reservoir simulations to field size reservoir simulations, to enhance knowledge of complicated flow behavior that is built and addressed using numerical, analytical, and semi-analytical reservoir models for unconventional reservoirs. However, in order to anticipate the performance of a shale gas reservoir, correct shale rock attributes must be included in order to construct a geologic model for the entire asset. The principal stress profile of an oil and gas reservoir is heavily influenced by the rock geomechanical characteristics. Poisson's ratio, total minimum horizontal stress, and bulk, Young, and shear modulus are all geomechanical parameters of reservoir rock. In comparison to conventional reservoirs with established adequate knowledge, these features play a considerable part in contemporary shale asset development plans. Furthermore, having access to geomechanical data can help engineers and geoscientists in shale gas fields with geomechanical modeling, hydraulic fracture treatment design, and reservoir simulation.

Geomechanical characteristics like as Young's modulus and compressive/tensile strength have traditionally been obtained by inference from wireline logs or, preferably, testing recovered core. Worden et al. (2020) said that core from shale units is rarely retrieved during traditional oil and gas developments [32]. Even when the core is recovered, obtaining good-quality shale samples required for normal mechanical testing is difficult due to the fact that it is frequently laminated and friable. Furthermore, shale can be readily damaged during drilling, core recovery, transportation, and storage [33, 34]. Robust geomechanical data on shale lithologies are, inevitably, scarce. Furthermore, due to sample preparation requirements, neither wireline logs nor core tests allow for clear characterisation of anisotropy, which can be considerable in shales and is critical for interpreting seismic reflection data [35]. Since the mid-2000s, researchers have been studying the mechanical characteristics of the Longmaxi shale components, which include grains of phyllosilicates, quartz, feldspar, carbonates, organic matter (OM), and pyrite. The microstructure is very diverse, with shale "building blocks" ranging in size from sub-micron clay plates to lenses and organic particles a few microns across to silt-size minerals. Nanoindentation testing and atomic force microscopy (AFM) (Charlton et al. Instead of depending on the recovery of full core, these micromechanical tests may be performed on tiny

DOI: 10.31695/IJASRE.2025.4.2

pieces of shale, such as drill cuttings or core fragments; this also improves the characterisation of shale anisotropy [36].

3.1. Geomechanical properties

3.1.1. Elastic properties

Young's modulus and Poisson's ratio are two important rock characteristics for determining the elastic deformation of rock formations. Young's modulus denotes the ratio of longitudinal stress to longitudinal strain, whereas Poisson's ratio denotes the ratio of longitudinal strain to lateral strain. These factors' values aid in determining the in-situ stresses operating on a rock formation at a certain depth [37], as well as how those rocks are anticipated to respond if the prevailing stress Beld changes. Poisson's ratio is the mathematical expression for the ratio of lateral strain to axial strain. (1). Young's modulus refers to the ratio of tensile stress to tensile strain eq. (2), bulk modulus relates to the ratio of hydrostatic stress to volumetric strain eq. (3) and shear modulus refers to the ratio of shear stress to shear strain eq. (4).

$$\upsilon = \frac{\varepsilon_{lateral}}{\varepsilon_{axial}} \quad (1)$$

$$E = \frac{\sigma_t}{\varepsilon_t} \quad (2)$$

$$k = \frac{\sigma_p}{\varepsilon_{vol}} \quad (3)$$

$$G = \frac{T}{\gamma} \quad (4)$$

In eqs. (1) – (4), ε lateral, lateral strain, ε axial, axial strain, σ_t, tensile stress, ε_t, tensile strain, σ_p, hydrostatic stress, ε vol, volumetric strain, T, shear stress and ϒ, shear strain. [38-40]

The requirement of two (2) elastic moduli for thorough description of material behavior is a crucial component of the elasticity theory of homogeneous, isotropic rock material. Shale is not an isotropic and homogeneous rock, contrary to what is commonly believed [41-43]. Shale shows anisotropy, in which its elastic characteristics change with direction [44, 45]. This anisotropy is brought on by significant differential stress, the alignment of minerals (clay and mica) along bedding planes, and macro-sized fractures and faults. Anisotropy is frequently ignored in calculations for rock elasticity, which can sometimes result in significant inaccuracies that make the results useless [39]. According to the mathematical formula in equation (5), each stress component in a generic anisotropic material is linearly connected to a separate coefficient and strain component.

$$\sigma_{ij} = C_{ijkl}\,\varepsilon_{kl} \quad (5)$$

where C_{ijkl}, elastic constants with the indices (i,j,k and l) taking the values (1,2 or 3) and resulting to 81 constants (C_{ijkl}). Based on elastic constants, three different materials can be characterized: (1) isotropic material by two elastic constants, (2) orthotropic material by nine elastic constants and (3) transverse isotropic material by five elastic constants [39, 40, 46].

In addition to vertical stress, a reservoir's depth is affected by horizontal in-situ stresses, which are defined by elastic properties like Young's modulus and Poisson's ratio. For the purpose of choosing the best borehole trajectory and fracturing scheme design for horizontal wells required for shale gas production, they represent the main in-situ stresses that are mutually perpendicular to one another and relevant [3]. The primary in-situ stresses are indicated by the letters S_V (vertical stress), also referred to as the overburden stress, S_{hmin} (minimal horizontal stress), and S_{Hmax} (maximum horizontal stress). Due to Poisson's ratio effects, the

DOI: 10.31695/IJASRE.2025.4.2

weight of the underlying rock formations and the fluids they contain causes vertical stress, which in turn causes the spreading and expansion of the underlying formations in horizontal lateral directions [47]. According to Adnoy and Looyeh (2011), the minimum and maximum horizontal stresses are created by the lateral movements caused by the overburden stress and the presence of adjacent rock materials [47].

To categorize different faulting regions (normal, strike-slip, and reverse faults), Anderson (1951) used the principal stresses, where (S_V) is the maximum principal stress in a normal fault, the intermediate principal stress in a strike-slip fault, and the least principal stress in a reverse fault [48]. The magnitude of the primary stresses used in Anderson's classification of the fault regions are shown in Table (1), with S_1 denoting the maximum, S_2 the intermediate, and S_3 the least primary stresses. In Fig. (4), fault regions and associated stress magnitudes are further diagrammatically depicted. For determining the primary in-situ stresses, various techniques have been used. In offshore locations, water depth is taken into account using equation (7), and vertical stress (S_V) can be calculated using the integral of rock densities from surface to targeted depth using equation (6) [49].

$$S_v = \int_0^z \rho(z) g dz \approx \bar{\rho} g z \tag{6}$$

$$S_v = \rho_w g z_w + \int_{z_w}^{z} \rho(z) g dz \approx \rho_w g z_w + \bar{\rho} g (z - z_w) \tag{7}$$

where ρ(z), density expressed as a function of depth (z), g, acceleration due to gravity ρ, mean of overburden density, ρ_w , water density taking as $1 g/cm^3$, and z_w ; water depth [40, 50]. Using both direct and indirect methods, Aadnoy and Looyeh (2011) described how to measure in-situ stresses [47]. The overcoring gauge test, the flatjack test, and the hydraulic fracture test were all parts of the direct approach. Borehole breakouts, differential strain analysis, fault plane solutions, acoustic emission, inelastic strain relaxations, and observations of discontinuity states make up the indirect method.

Table 1: Stress magnitude of different Fault regions [40].

FAULT REGIONS	**STRESSES**		
	S_1	**S_2**	**S_3**
Normal	S_V	S_{Hmax}	S_{hmin}
Strike-Slip	S_{Hmax}	S_V	S_{hmin}
Reverse	S_{Hmax}	S_{hmin}	S_V

The isotropic and anisotropic models are now utilized to calculate the magnitude of horizontal stresses (minimum and maximum). The isotropic model implies that elastic parameters in a homogeneous intact rock do not change in any direction, but the anisotropic model posits that elastic parameters change with direction in an anisotropic heterogeneous rock, such as a shale gas reservoir [51, 52].

DOI: 10.31695/IJASRE.2025.4.2

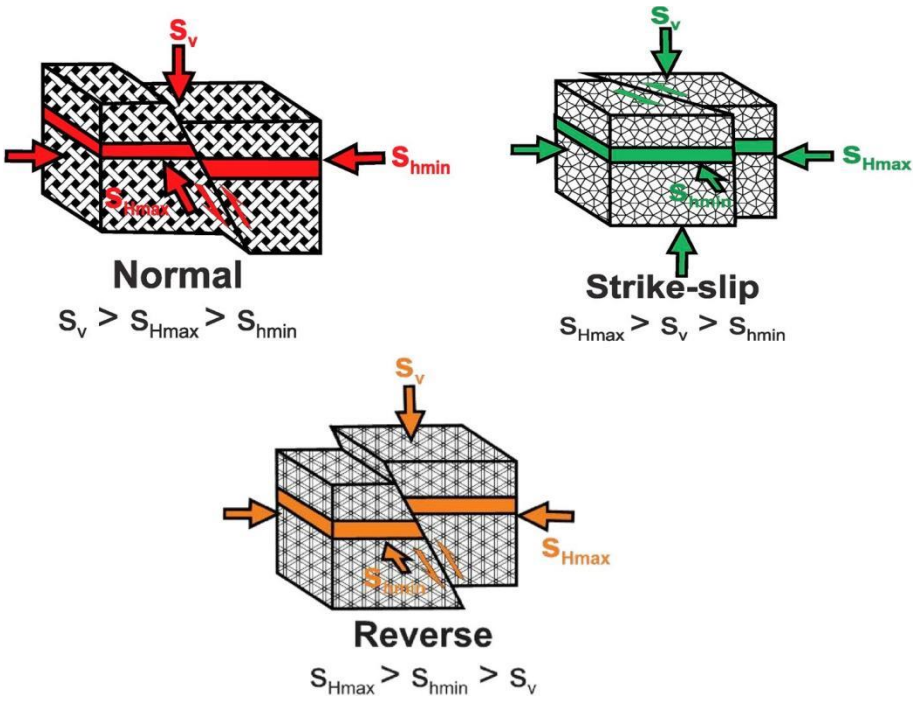

Fig. 4. Distribution of principal in-situ stresses (S_v, S_{Hmax} and S_{hmin}) and resulting fault regions (Normal, Strike-slip and Reverse) based on magnitude and orientation of the different stresses [53].

The equations (8) and (9) are used to calculate minimum and maximum horizontal stresses under isotropic conditions, whereas the equations (10) and (11) are used to forecast minimum and maximum horizontal stresses in anisotropic conditions.

$$\sigma_{h\min} - \alpha P_p = \frac{\upsilon}{1-\upsilon}(\sigma_v - \alpha P_p) + \frac{E}{1-\nu^2}\varepsilon_h + \frac{E\nu}{1-\nu^2}\varepsilon_H \quad (8)$$

$$\sigma_{H\max} - \alpha P_p = \frac{\upsilon}{1-\upsilon}(\sigma_v - \alpha P_p) + \frac{E}{1-\nu^2}\varepsilon_H + \frac{E\nu}{1-\nu^2}\varepsilon_h \quad (9)$$

where E is the Young's modulus, Poisson's ratio, v is the vertical overburden stress, Pp is the pore pressure, and biot's constant, and (h_{min} and H_{max}) are the minimum and maximum horizontal stresses, and (h and H) are the minimum and maximum horizontal strains [52, 54]. In eqs. (10) and (11), the subscripts (vert) and (horz) signify vertical and horizontal, respectively, and, the poroelastic constant [51].

$$\sigma_{h\min} - \alpha P_p = \frac{E_{horz}V_{vert}}{E_{vert}(1-\nu_{horz})}(\sigma_v - \alpha(1-\xi)P_p) + \frac{E_{horz}}{1-\nu_{horz}^2}\varepsilon_h + \frac{E_{horz}\nu_{horz}}{1-\nu_{horz}^2}\varepsilon_H \quad (10)$$

$$\sigma_{H\min} - \alpha P_p = \frac{E_{horz}V_{vert}}{E_{vert}(1-\nu_{horz})}(\sigma_v - \alpha(1-\xi)P_p) + \frac{E_{horz}}{1-\nu_{horz}^2}\varepsilon_H + \frac{E_{horz}\nu_{horz}}{1-\nu_{horz}^2}\varepsilon_h \quad (11)$$

3.1.2. Strength and failure properties

The capacity of a rock to sustain force without succumbing or breaking is represented by its strength. The mineralogy of rock particles and the behavior of particle interactions determine rock strength [55]. These qualities were formed as a result of the numerous processes of deposition, diagenesis, and catagenesis that led to the development of the rock, which were then modified by folding, faulting, fracturing, jointing, and weathering. The strength of a rock material is always characterized by its tensile, compressive, and shear strengths when considering the three (3) fundamental stress situations (tensile stress, compressive stress, and shear stress) [38]. Compressive strength is an important strength for reservoir rocks since it is important in

DOI: 10.31695/IJASRE.2025.4.2

determining well-bore stabilities, and the two most popular experimental approaches for determining it are uniaxial and triaxial compression testing.

The following mechanisms were listed by Aadnoy and Looyeh (2011) as having the potential to cause wellbore instability issues and formation rock failure: (1) tensile failure, (2) shear failure, (3) compressive failure, (4) plastic deformation, (5) cohesive failure, and (6) creep failure [47]. Tensile, shear, and compressive failures are the most prevalent of these. When the effective tensile stress acting across the plane of a rock mass exceeds the critical limit of tensile strength, tensile failure occurs. Tensile failure of a rock mass results in splitting along one or more fracture planes. According to Fjaer et al. (2008) and Nygrd et al. (2006), shear failure happens when shear stress along a plane in a rock mass exceeds the shear strength, a fault zone forms along the failure plane, and relative side movement of the failed plane occurs as a result of friction [39, 56]. When stresses acting on a rock mass exceed its compressive strength, compressional failure of the rock occurs. In this mode, failure is catastrophic, especially when the rock mass is brittle, but occurs gradually when the rock mass is ductile.

The strength of a rock mass is determined by two factors: rock matrix strength and rock discontinuity strength (cracks, joints, and fractures) [57]. For the failure analysis of intact rock masses based on two or three primary stresses, a number of failure criteria and constitutive models have been used: (maximum (σ_1), intermediate (σ_2) and minimum (σ_3)).

Failure envelopes are created using the failure criteria and are frequently linearized to distinguish between safe and failed regions in a rock mass. The various failure criteria applied to gauge the durability of uniform, intact rocks include: (1) Hoek-Brown, (2) Mohr-Coulomb, (3) Modified Lade, (4) Modified Wiebols-Cook and (5) Drucker-Prager. Hoek-Brown and Mohr-Coulomb are mostly used due to simplicity and extended application to rock masses but there is complete negligence of intermediate principal stress unlike in the case of Drucker-Prager, Modified Lade and Modified Wiebols-Cook failure criteria [40, 58, 59]. These criteria' failure envelopes (Fig. 13) are depicted in a three-dimensional stress space as follows: The failure envelope for Hoek-Brown and Mohr-Coulomb is a hexagonal pyramid; for Modified Wiebols-Cook and Modified Lade, it is a cone; and for Drucker-Prager, it is a circle [58, 59]. The Mohr-Coulomb failure envelope has two components that make up the Drucker-Prager failure envelope (inscribed on the inside and circumscribed on the outside; see Fig. 13). Rock failure has already occurred if the stress states that characterize the rock at the failure point, touch the failure envelope, or exceed the failure line.

According to Ismael et al. (2017) and Zoback (2007), the existence of weak bedding planes in shaley rocks has a major impact on rock strength [40, 60]. This influence is referred to as anisotropic strength and is dependent on the relative weakness and orientation of the bedding plane to the applied stresses. Donath (1961) and Jaeger and Cook (1979) established eq. (12) for the failure criteria of anisotropic rock materials with weak bedding planes [61, 62].

$$\sigma_1 = \sigma_3 \left[\frac{2(S_w + \mu\sigma_3)}{(1 - \mu \cot \beta_w)\sin 2\beta} \right] \qquad (12)$$

where S_w is the cohesive strength of the weak bedding plane, w is the internal friction coefficient of the weak bedding plane, w is the orientation of the weak bedding plane to the applied force, and is the failure angle of an undamaged rock [62].

In the rock strength testing experiment of rock samples were exposed to confinement pressures of (0, 20, and 35 MPa) and axial stresses (Fig. 5) [63].

DOI: 10.31695/IJASRE.2025.4.2

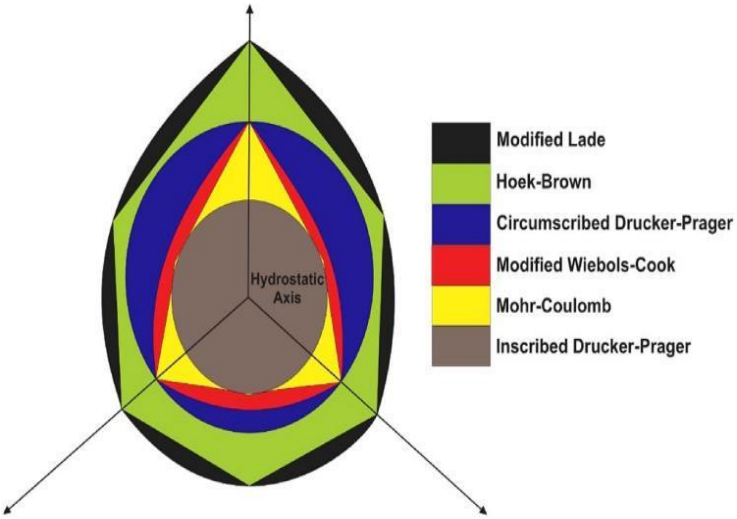

Fig. 5. Failure envelopes projected in a 3-dimensional space for Modified Lade, Hoek-Brown, Mohr-Coulomb, Modified Wiebols-Cook and Druker-Prager (subdivided into two: circumscribed (on the outside) and inscribed (on the inside) of Mohr-Coulomb envelope) [53, 63, 64].

3.2. Relationship between geomechanical properties and mineralogy of longmaxi shale in the burial evolution history

Characterizing the link between geomechanical characteristics and mineralogy, according to Ayonma Wilfred Mode et al (2022), is critical for predicting brittle intervals, which impact the incidence and distribution of natural fractures, as well as the rock's reaction to hydraulic fracturing [65]. The brittleness of Longmaxi Shale samples was assessed using mineralogical features to determine which component had the most effect on the shale's brittleness. XRD analysis classified minerals into non-clay and clay groups, with quartz and calcite in the non-clay class and illite, muscovite (mica), and kaolinite in the clay class. Additionally, Shi Xian et al. (2019) used dot matrix nanoindentation measurements to examine the mechanical properties of Lower Silurian Longmaxi shale samples from Youyang, including Young's modulus, hardness, and fracture toughness [66]. According to their experimental findings, Young's modulus and hardness are positively correlated, as are Young's modulus and fracture toughness at the nanoscale. However, Young's modulus, hardness, and fracture toughness that are perpendicular to the bedding are slightly lower than those that are parallel to the bedding. For instance, the Young's modulus of rock samples with parallel beddings ranges from 35.61 GPa to 59.47 GPa at its highest value. The highest value is 1.67 times greater than the lowest value. The samples' heterogeneity is the cause. In order to determine the degree of uncertainty in the test results for nanoindentation, statistical analysis is required. Wei-bull model can effectively characterize heterogeneity and mechanical response features of rock under external force, according to previous studies on the distribution of rock mechanical parameters. More importantly, it is simple to measure the parameters of this model [67, 68].

Yunzhong Jia et al. (2021) also applied the axial stress using the circumferential displacement control mode at a rate of 0.015 mm/min until the sample failed [69]. They came to the conclusion that as the phyllosilicate content of the longmaxi shale increased, so did the elastic modulus and uniaxial compressive strength. The uniaxial compressive strength decreases as phyllosilicate content rises, and this could be because phyllosilicate minerals have a weakening effect on the mineral bond. The elastic modulus significantly decreases as phyllosilicate content rises. They show how the phyllosilicate content, tensile strength, and uniaxial compressive strength/tensile strength ratio of four different types of shales relate to one another in Fig. 6. The amount of phyllosilicate content decreases with increasing tensile strength [70]. According to earlier studies, the ratio of uniaxial compressive strength to tensile strength for the same type of rock nearly

DOI: 10.31695/IJASRE.2025.4.2

remains constant) [71]. According to their research, the ratio of shale tensile strength to uniaxial compressive strength ranges from 10.23 to 13.80, meaning that shale tensile strength is almost 10% of uniaxial compressive strength. The microstructure and macroscopic geomechanical properties of shale, including its elastic modulus, tensile strength, and uniaxial compressive strength, are strongly influenced by its mineralogical composition, according to experimental results. In Longmaxi shale, which has a higher concentration of phyllosilicate minerals, there are numerous organic pores and micro-fractures that serve as shale gas storage locations and communication pathways between hydraulic fractures to increase matrix permeability. Additionally, the uniaxial compressive strength, triaxial strength, elastic modulus, and tensile strength of the shale with higher phyllosilicate mineral content are reduced.

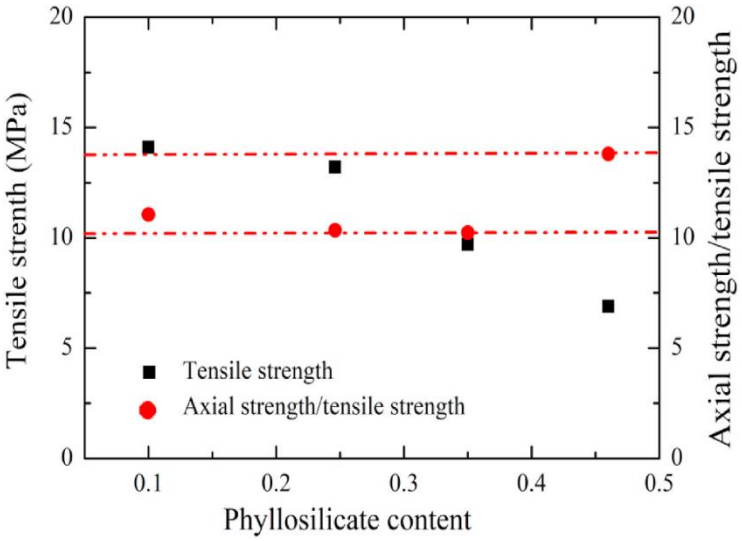

Fig.6: The link between phyllosilicate concentration, tensile strength, and axial strength/tensile strength in four different types of shale samples. Tensile strength falls as phyllosilicate content increases. In a narrow range, the axial strength/tensile strength varies from 10.23 to 13.80.[69]

By using the nanoindentation method, Yiyu Lu et al. (2022) investigated the differences in the micromechanical properties of shales from various depositional environments of the Longmaxi marine shale [69, 72]. The results demonstrate that while the elastic modulus of the marine and continental shale samples is similar, the latter has a higher hardness (fig. 7). Similar mineralogy may be the cause of the two shale samples' similar elastic moduli. The marine shale sample forms a clay support matrix while the continental shale sample forms a rigid clastic support matrix as a result of differences in deposition and diagenesis. As a result, the former has lower hardness while the latter has higher hardness. The clay support matrix and low hardness of the shale suggest that more serious proppant embedment problems may arise. According to the findings, the marine shale samples' elastic modulus ranges from 34.97 to 48.91 GPa with an average of 44.70 GPa, and their hardness varies from 1.19 to 1.91 GPa on average. The continental shale samples have an elastic modulus that ranges from 25.55 to 80.27 GPa on average and a hardness that varies from 0.92 to 9.25 GPa on average. They noticed that the clay matrix is prone to plastic deformation when the indenter intrudes, which inadequately restrains the movement or rotation of the hard embedded minerals. The formation of a weak bearing structure in marine shale and poor resistance to the penetration of indenters (i.e. low hardness) are caused by the tendency of hard minerals to dislocate with the dislocation of clay minerals. The hard minerals in continental shale, on the other hand, are larger and more densely packed, which limits their rotation or movement during indented penetration and creates a rigid bearing structure. As a result, the continental shale has a high hardness and a low ability to be penetrated by an indented. To explain how microtexture and particle size affect shale hardness, a condensed conceptual model is proposed (Fig. 8).

DOI: 10.31695/IJASRE.2025.4.2

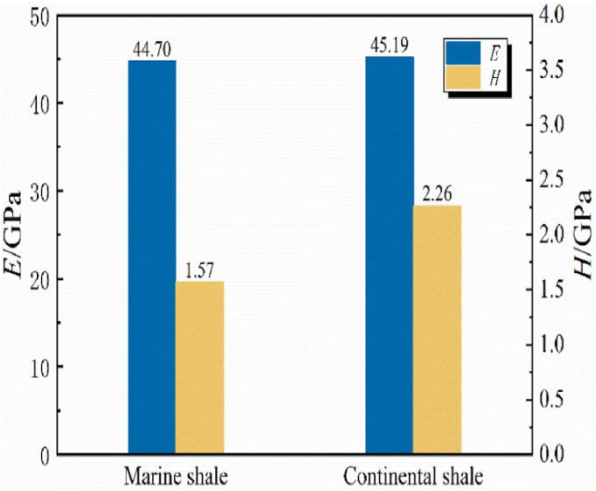

Fig. 7. (a). Average elastic modulus and average hardness of marine shale and continental shale.[73]

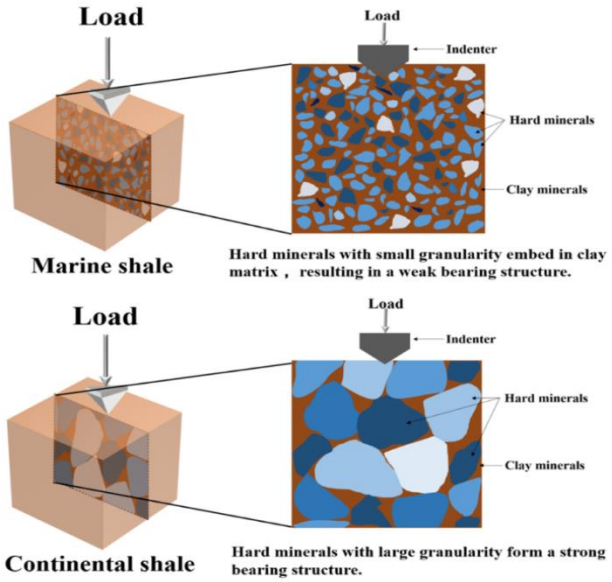

Fig.8: A simplified conceptual model to explain the effect of microtexture and particle size on shale hardness. [73]

When Yaper Ye et al. (2022) looked into the effect of mineral compositions on the brittleness of the Longmaxi shale, the results showed that clay minerals and quartz are the typical plastic and brittle minerals, respectively [74]. It makes sense that the amount of clay minerals in shale samples is negatively correlated with BI (R^2 = 0.82, Figure 9a), as the energy absorbed from loading is primarily dissipated through the plastic deformation of clay minerals. High plastic energy (Wp) and low BI are characteristics of rocks with a high clay mineral content (Figure 9b). In shale samples, the presence of brittle minerals positively correlates with BI (Figure 9c). The energy absorbed during compression is primarily converted into elastic energy, which causes cracks to form in rocks with a high proportion of brittle minerals (Figure 9d). This type of rock has a high BI because fracture networks can form when cracks spread along brittle minerals.

DOI: 10.31695/IJASRE.2025.4.2

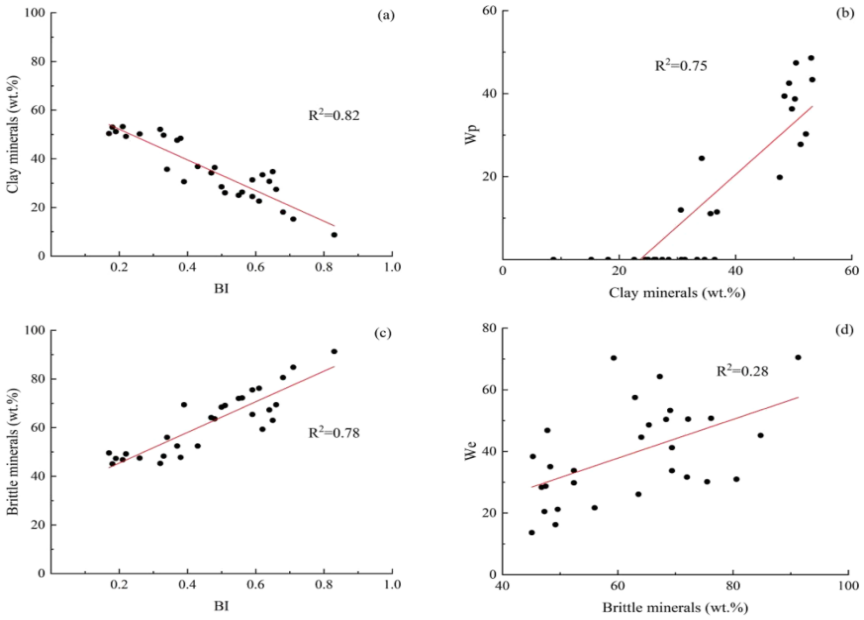

Figure 9. Relationships between BI, various minerals, and brittleness characteristic parameters of shale samples from the Wufeng−Longmaxi formations. BI, brittleness index; We, consumed elastic energy; and Wp, plastic energy. [74]

Accordingly, brittle minerals can be divided into micron-size (2 m) microcrystalline quartz and silt-size (>2 m, 62.5 m) brittle minerals (terrigenous quartz, feldspar, and authigenic carbonate minerals). The relationships between BI and these two minerals in different sizes show that the contribution of brittle minerals isolated in the shale matrix to shale brittleness is small, whereas the abundant micron-size microcrystalline quartz in the shale matrix can connect the silt-size brittle minerals to form amphiboles. Additionally, the following relevance levels between energy-based BI and rock minerals were determined through gray relational analysis: Micron-size microcrystalline quartz content (γ = 0.48) is significantly higher than terrigenous feldspar (γ= 0.37), terrigenous quartz (γ = 0.33), clay minerals (γ= 0.30), and carbonate minerals (γ= 0.22), suggesting that it significantly contributes to shale brittleness. Biogenic quartz and SI quartz make up authentic quartz.

4. THE RELATIONSHIPS BETWEEN GEOCHEMICAL PROPERTIES AND MINERAL COMPOSITION OF SHALE

4.1. The impacts of mineral composition on TOC of Longmaxi shale

According to Wenming Ji et al. (2020), who demonstrated the existence of a weakly positive relationship between TOC and pyrite contents (Fig. 10a), low oxygen content is crucial for better organic matter preservation [75]. However, the Longmaxi Formation exhibits significant vertical TOC heterogeneity. Although it appears that the lower Longmaxi member was deposited in an anoxic to euxinic environment, it has a low TOC content. Furthermore, the upper member exhibits a significant accumulation of organic material, despite the fact that these organic-rich shales were deposited in a suboxic environment. These phenomena suggest that redox conditions are significant but not the dominant factor. It is obvious that the overwhelming benefits of organic production over destruction may have also aided in the accumulation and enrichment of organic matter. Additionally, clay and feldspar contents have weakly negative relationships with TOC contents (Fig. 10c and d), suggesting that terrigenous dilution is primarily responsible for controlling the accumulation of organic matter. According to the findings discussed above, the most important factor influencing the accumulation of organic matter is the dilution of terrigenous detritus from

DOI: 10.31695/IJASRE.2025.4.2

the Xuefeng Uplift under pervasive high production and reducing conditions. They also observed a strong positive correlation between the TOC content and the brittleness index [76].

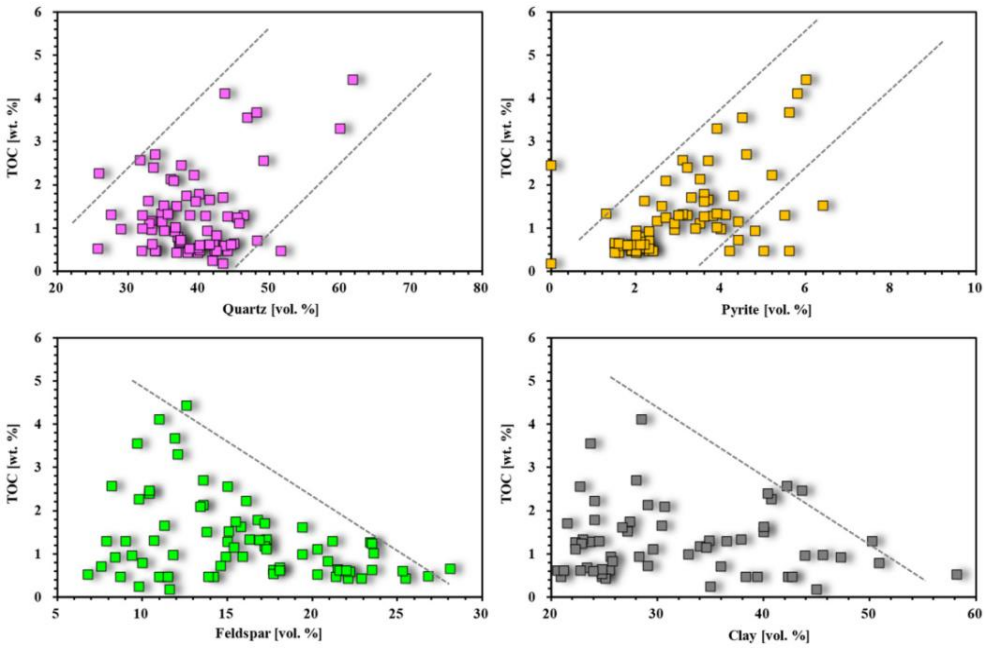

Fig. 10. The relationships between TOC and mineral composition of the lower Silurian Longmaxi shale in the southeastern Chongqing area. Gray dotted line is envelope curve of scatter plot. [75]

Additionally, Boning Zhang et al. (2020) created a review on the formation and gas characteristics of shale gas reservoirs, and they calculated the TOC content using samples that had been ground into a powder with a particle size of less than 100 mesh and a CS230 carbon/sulfur analyzer (LECO, St. Joseph, USA) [18]. Hydrochloric acid is used to dissolve the inorganic carbon after the powder is pyrolyzed up to 600 C. The connection between quartz and TOC content can be used to determine whether quartz is detrital or biogenic in origin. They concluded that biogenic quartz and TOC can be correlated positively, whereas there is no linear relationship between detrital quartz and TOC content. As seen in Figure 11, the quartz in the targeted formation is biogenic because the correlation coefficients between quartz and TOC content in the X1, X2, and X3 wells are all greater than 0.53.

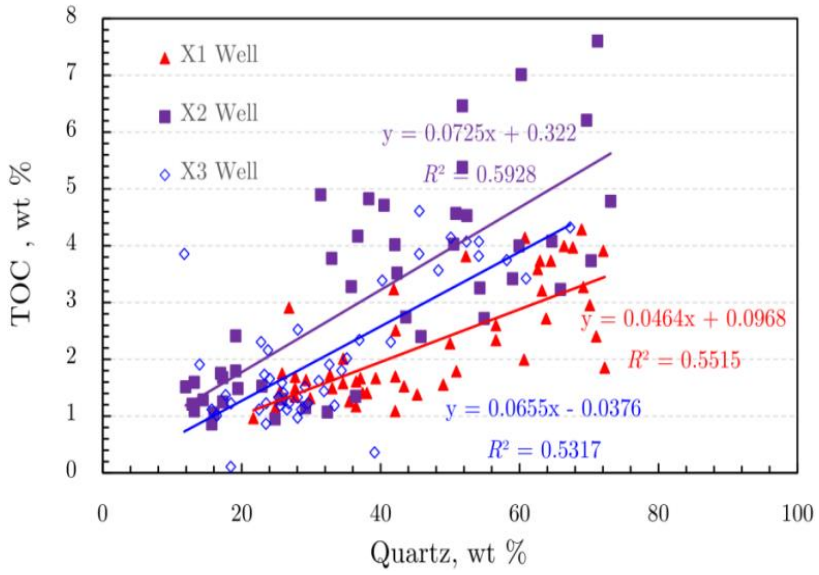

Figure 11. The relationship between quartz and TOC contents in Longmaxi Formation. [18]

DOI: 10.31695/IJASRE.2025.4.2

Also, clay and siliceous minerals were tested to see how they affected the TOC content of longmaxi shale by Bingqiang Chai et al in 2023 [77]. The TOC has a good positive correlation with siliceous mineral content and a good negative correlation with clay mineral content, they found (Figure 12a,b). The higher the TOC content, the higher the siliceous content and the lower the clay content. The study area's lithofacies are primarily siliceous shale when the TOC is greater than 4.0%, clay siliceous shale, calcareous siliceous shale, and siliceous shale when the TOC is between 3.0 and 4.0%, and siliceous shale when the TOC is between 2.0 and 3.0%. The lower limit of the TOC content of the advantageous lithofacies shale reservoir in the mountain shale in the Longmaxi shale is 2.0% because the TOC must be greater than 2.0% for a shale reservoir to be a potential target for industrial exploitation.

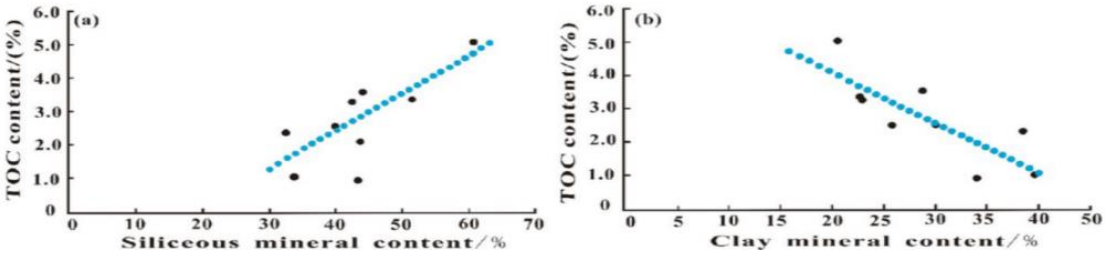

Figure 12. Relationship between TOC content and (a) siliceous mineral content and (b) clay mineral content. [77]

4.2. Rock-fluid reaction in the fracturing, production, and storage of longmaxi shale.

4.2.1. Pore types and morphology

According to Cunhui Fan et al. (2020), the shale gas is primarily present in two states: in the free state in the pore space and in the adsorbed state on the surfaces of the mineral particles [78]. They can be classified into inorganic pores, organic pores, and microfractures based on their differences [79, 80]. Shale contains a variety of inorganic pores and minerals with a complex mineral composition. The interior of the rock also has clay interlayer pores, mineral edge fractures created by compaction, and microfractures as a result of the accumulation of clay minerals. They are the primary organic pores and hydrocarbon-generating shrinkage pores develop in shale as a result of the high thermal evolution of shale organic matter [81]. Recently, there has been a lot of interest in the economy regarding the nanopores and micropores in fine-grained sediments. However, it can be very difficult to define these pores. According to Loucks et al. (2009), nanopores have a diameter of less than 0.75 nm, while micropores have a diameter of around 0.75 nm [82]. Shale nanopores fall into two different categories. According to Rouquerol et al. (1994), one common classification for these pores is micropores (2 nm), mesopores (2–50 nm), and macropores (>50 nm) [83]. Secondly, organic matter (OM) pores, interpore pores, and intrapore pores can all be classified as pores. To describe shale gas reservoirs and comprehend the pore properties of shale, both classifications are combined. The FIB-SEM and FE-SEM pore imaging techniques directly characterize the type and morphology of organic and inorganic pores. Shale textural and structural properties have been the subject of extensive research since a recent successful shale gas exploration. This study revealed that shale may have significant pores and thus may serve as a significant in situ gas reservoir [82]. According to their size, micropores (pores with a diameter greater than 0.75 um) and nanopores (pores with a diameter less than 0.75 um) can be distinguished as two general categories of pores in shale. Both intraparticle and interparticle types of micropores exist. Silica has largely displaced fossils in the Longmaxi Formation. Additionally, when certain minerals, such as carbonates, quartz, feldspars, and a suite of heavy minerals, become partially or completely dissolved, micropores are created. They estimate that the Longmaxi Formation shale may contain about 2% of the nanoporosity based on SEM analysis of the sample. In the Sanxing 1 well of the

DOI: 10.31695/IJASRE.2025.4.2

Longmaxi Formation black shale, SEM analysis reveals the presence of a variety of intragranular micropores in calcite, dolomite, and quartz, as well as dissolution pores in plagioclase and micaceous lamellar pores in clays. The later pores have a size range of 100 nm to 50 m. Furthermore, pore structures in shale formations may be separated into two categories, according to Boning Zhang et al (2020): matrix pores and fractures [18]. The major storage area of shale gas is matrix pores, which directly determine the reserve of a shale gas resource. The ability to transport and produce gas is determined by the formation of fractures as well as the connection of pores.

Minerals with strong anti-compaction properties include quartz, feldspar, and pyrite. Mineral particles can also support one another to form intergranular pores [84]. The majority of these pores (Fig. 13a) have slit- or wedge-shaped shapes and range in size from 50 nm to 100 nm. The intragranular pores, which have pore sizes ranging from 5 nm to 70 nm, are present in the original mineral particles and are unaltered during the late stages of sedimentary diagenesis. With pore sizes ranging from 10 nm to 200 nm, the intercrystalline pores are primarily found between pyrite crystals or clay minerals (Fig. 13b and c). Selective dissolution of diagenetic minerals, which are primarily elliptical and asymmetrical in shape, creates the dissolution pores. The strength of the dissolution has an impact on the pore size range, which is primarily distributed between 20 nm and 600 nm. The target layer's shale contains a significant amount of pyrite, some of which dislodge due to dissolution and create moldy pores (Fig. 13d and e). Primary organic pores and pores that generate hydrocarbons are included in the organic pores. Shale depth, organic matter type, and thermal evolution are all closely related to the degree of organic pore development. Argon-ion-polished scanning electron microscopy revealed that there are numerous black organic particles with spot- and band-like distributions, as well as numerous organic pores that have developed inside that are circular, elliptical, and honeycomb-shaped (Fig. 13g). The high-quality shale intervals' organic matter is primarily type I kerogen. The shale is highly mature, and shrinkage pores that can form hydrocarbons have formed. It is possible to see organic pores that are circular, elliptical, and honeycomb-shaped, with pore sizes that range from 2 nm to 200 nm (Fig. 13h). The high-quality shale of the Wufeng and Longmaxi Formation has many different types of fractures, including mineral edge fractures formed between various mineral contact surfaces (Fig. 13i) and fractures brought on by tectonic stress (Fig. 13f). This is evident from core and microscopic observations.

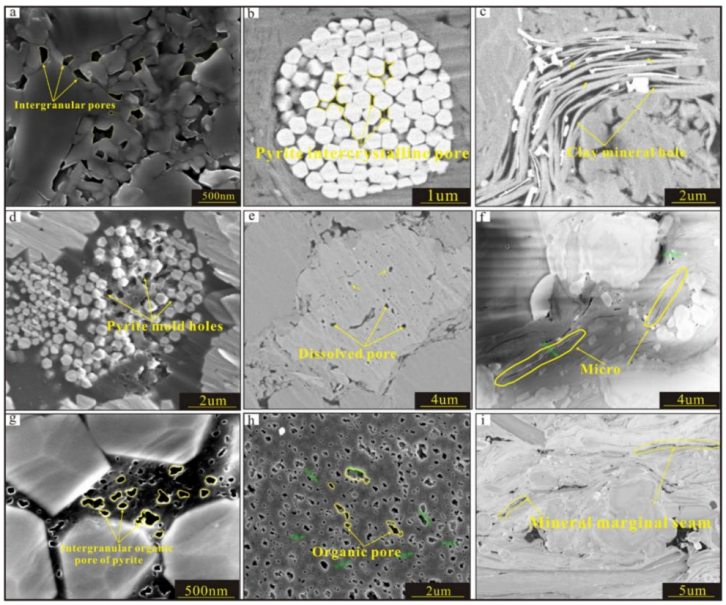

Fig. 13. Microscopic pore types of Wufeng and Longmaxi Formation in the study area. a. 2049.02 m, Longmaxi Formation, DY1; b, c. 2052.96 m, Longmaxi Formation, DY1; d. 4364.75 m, Wufeng Formation, DY1; e. 4 360.5 m, Longmaxi Formation, DY2; f. 3763.83 m, Longmaxi Formation, DY5; g. 2030.00 m, Longmaxi Formation, DY1; h. 3776.29 m, Longmaxi Formation, DY5; i. 3812.34 m, Longmaxi Formation, DY5.

DOI: 10.31695/IJASRE.2025.4.2

When Xueyuan Li et al. (2022) investigated the impact of pore structure specificity and pore water on the occurrence of deep shale gas from the Wufeng-Longmaxi Formation, they found that both organic and inorganic pores, including organic matter pores, intragranular pores, intergranular pores, and microfractures, are well developed in the deep shale gas reservoir (Fig. 14) [85]. One of the most developed pore types, organic matter nanopores have a wide range of sizes, shapes, and pore connectivity (Fig. 14a, b, and c). The majority of organic matter pores are found in the mineral frameworks of pyrite (Fig. 14b), quartz (Fig. 14a and e), and clays. Furthermore, because organic matter is so highly adsorbable, organic matter nanopores serve as the most significant repository for deep shale gas. The majority of intragranular pores are found in dolomite (Fig. 14d) and quartz (Fig. 14e and f) and typically form inside mineral grains. In deep shales, these pores make up a small percentage and are frequently isolated in minerals. In the deep shale under study, intergranular pores of various sizes and complex shapes were widely developed. Intergranular pores in clay minerals and quartz were the most frequently found. In contrast to intragranular pores, which are more important for reservoir fluid storage, migration, and seepage, intergranular pores typically have larger pore sizes, better connectivity, and greater quantity. Numerous microfractures, including stress-induced microfractures (Fig. 14c) and interlayer fractures in clay minerals (Figs. 14a and f), were also discovered in the deep shale under study in addition to pores. Microfractures serve as a link between macrofractures and micropores, greatly improving reservoir connectivity and creating interconnected seepage networks.

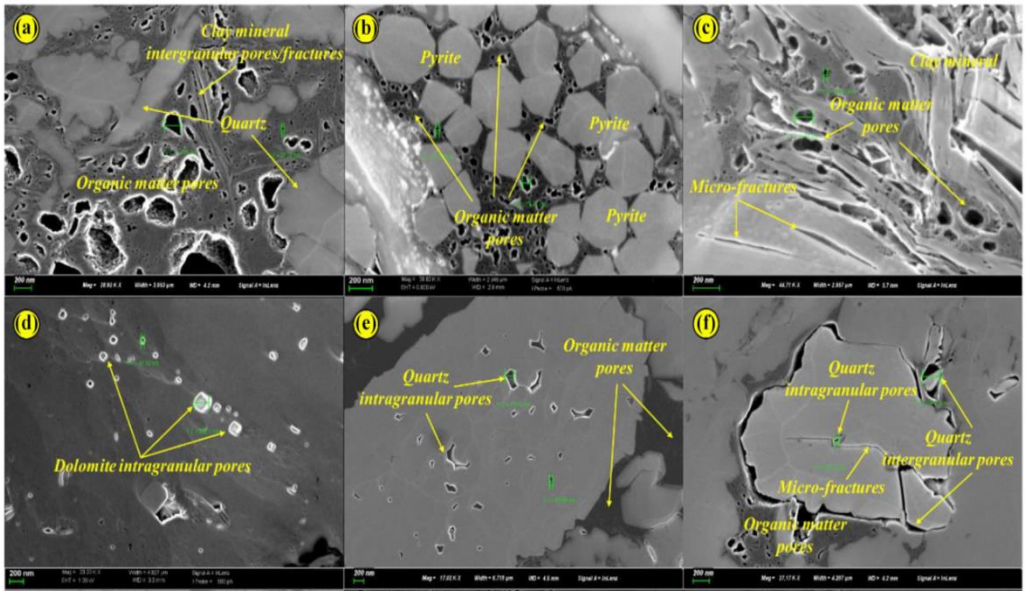

Fig.14: SEM images of deep shale samples. See text for explanations. [85]

4.2.2. Factors affecting pore structure characteristics

Pores connected to both organic and inorganic particles make up the pore network in shale that is rich in organic material. According to Yang et al. (2017), each shale formation has a distinct tendency to produce a pore system that is influenced by the quantity and thermal maturity of mineralogy and organic matter [86]. Pore structure, in turn, depends on primary and secondary pore development, which in turn depends on reservoir quality. Organic matter-related pores are regarded as secondary pores. According to Löhr et al. (2015, the pore network in shale is typically controlled by the organic contents and maturity. To explain organic pores, there are two theories [87]. First, when organic matter was still juvenile and nonporous, the primary organic pores formed [88]. According to second concepts, when organic matter is present as porous or spongy material as mature kerogen, thermal maturation generated pores in the organic matter [87]. Micropores and mesopores in thermally matured organic materials have been seen in numerous. Shale at its embryonic stage has a diverse distribution of organic matter and inorganic mineral aggregates. Additionally,

DOI: 10.31695/IJASRE.2025.4.2

earlier research shown that pyrolysis results in a 35% loss of organic carbon and an increase in net effective porosity of 4.9% [89].

4.2.2.1. Relation between pores structures and TOC

Organic matter content quantifies source rock potential and influences shale pore structure. Previous research has shown that TOC plays an important role in the development of pores linked with organic matter [90]. In marine shale, a high TOC promotes pore growth, but in transitional shale, there is no association between TOC and pore development. By comparing the bulk density of the rock with the average grain density calculated from the combination of TOC and XRD mineralogy data, Jixin Deng et al. (2014) estimated the porosity of the shale samples [91]. The relationship between porosity, TOC, and clay content is depicted in Figures 15(a) and (b), respectively. In each section, they found a positive correlation between porosity and TOC volume and a negative correlation between clay volume and TOC volume. These findings demonstrate that the porosity or reservoir space of the Wufeng-Longmaxi shale is primarily determined by the TOC. More organic matter pores may develop as a result of hydrocarbon generation when the TOC volume is higher. A higher TOC volume also indicates a higher quartz content, which can partially offset the effects of compaction and maintain the pores of the organic matter.

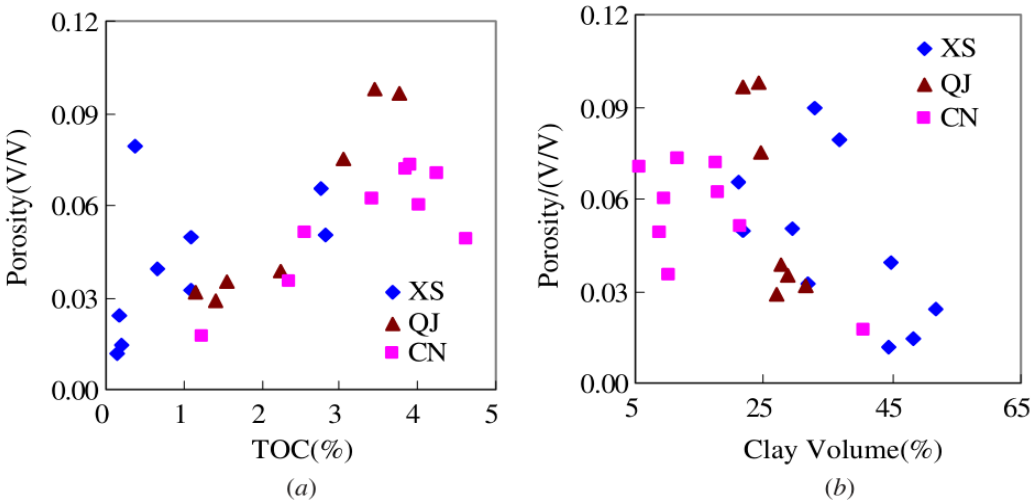

Fig.15: Crossplot of the TOC, clay volume and porosity of the Wufeng–Longmaxi shale. (a) TOC versus porosity, (b) clay volume versus porosity. [91]

In order to study the pores of the Longmaxi Formation quantitatively, Xueyuan Li et al. (2022) calculated the proportions of micropores, mesopores, and macropores (Fig. 16) [85]. They discovered that while the micropores and macropores were less developed in the deep shale, mesopores were mostly developed. Between 2.67 and 18.51% of pores are micropores, with an average of 13.10%; between 69.16 and 85.69% of mesopores, with an average of 75.05%; and between 9.44 and 14.28% of macropores, with an average of 11.85%. More mesopores are present specifically in the lower portion of the Longmaxi Formation (Y8) and the upper portion of the fourth bed (Y2). The trend of micropores, in contrast, was the exact opposite of that of mesopores. Overall, as burial depth increased, the proportion of macropores first rose and then fell. According to a comparison study done by Haijiao Fu et al. in 2022, quartz content is positively correlated with micropore surface area, micropore volume, and BET surface area, but negatively correlated with average pore diameter, which is in line with the relationship between the TOC content and the aforementioned parameters [92]. Due to quartz's biogenic origin, the analysis shows that its effects on pore structural parameters are comparable to those of TOC content. However, there is no clear relationship between the clay content and the parameters governing pore structure, suggesting that clay minerals have little impact on the pore structure of marine shale. The main explanations for this could be that (1) the

DOI: 10.31695/IJASRE.2025.4.2

influence of Organic Matter pores on pore structure is too strong in marine shale, weakening or hiding the correlation between clay content and pore structure, and (2) the clay minerals are composed of various types of minerals, such as kaolinite, illite, and chlorite, which may contain various types of pores and prevent a clear relationship from emerging.

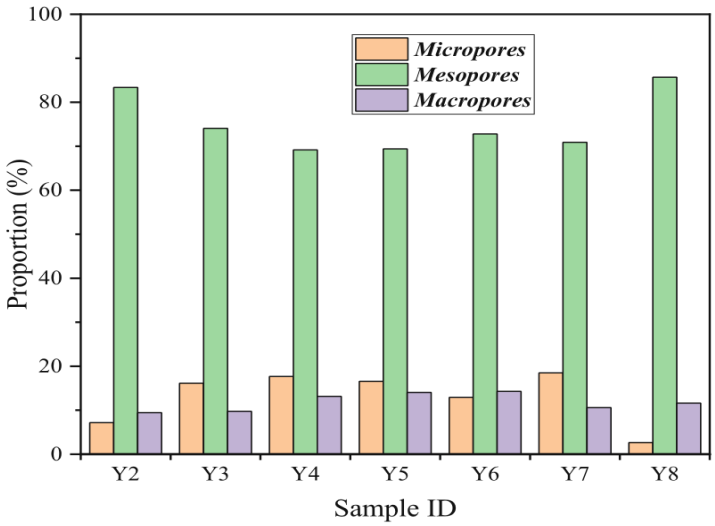

Fig.16: Proportion of different pore size sections. [85]

In order to characterize the pore structure and pore water microscopic migration in deep shale gas reservoirs of the Wufeng-Longmaxi Formation, Xueyuan Li et al. (2022) also conducted nuclear magnetic resonance experiments [92]. The results showed that the TOC content was weakly positively correlated with the proportion of micropores (Fig. 17a), while it was negatively correlated with the proportion of mesopores (Fig. 17b). The proportion of micropores increases and the proportion of mesopores decreases with increasing TOC content. These show that in the deep shale gas reservoir under study, organic matter primarily produced micropores while inorganic minerals primarily produced mesopores. This result is in line with those of numerous studies on the pore structure of shallow shale gas reservoirs, which have shown that organic pores typically have much smaller pore sizes than inorganic pores [18, 93]. Tonglou Guo et al. (2023) carried out systematic experimental characterisation of pore structures and sorption in deep shales from the Wufeng-Longmaxi Formations [94]; the effects of TOC concentration on different pore structure parameters of shale samples are shown in Fig. 35. They observed that the micropore volume was positively associated to the TOC content (Fig. 18a), but the macropore volume and the TOC content had no discernible association (Fig. 18b). As a result, shales with greater TOC concentration have larger micropore volumes.

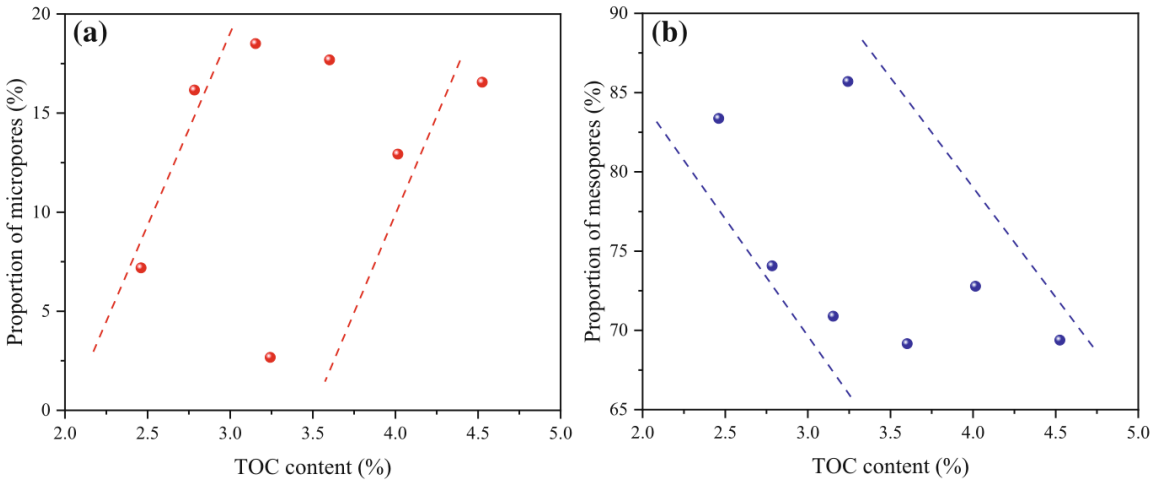

DOI: 10.31695/IJASRE.2025.4.2

Fig.17: Relationships of TOC content with the proportions of (a) micropores, (b) mesopores) [85]

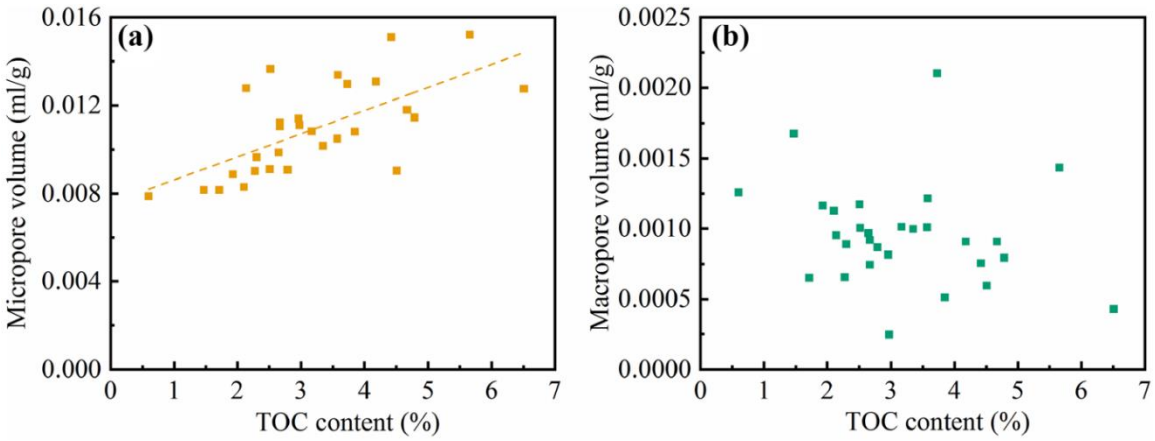

Fig.18: Effect of TOC contents of the shale samples on their: (a) micropore volume; (b) macropore volume. [94]

4.2.2.2. Correlation between shale mineral composition and pore structure

To observe the impact of mineral composition on the pore-development process, several correlations were developed. Previous research has shown how composition affects pore development. Conclusions based on scientific evidence, however, differ widely and are attributed to various types of shale all over the world. Because of the intricate crystal structure of clay minerals, some studies have shown that they have a detrimental effect on the growth of pore networks in shale [95, 96]. The homogeneous nature of pores could also be caused by more adsorbed water than organic matter. In addition, it has been suggested that clay minerals may allow pores to collapse under intense compaction in strata that are deeply buried [97, 98]. The pores developed in clay are all long strips with lengths of 0.2-2 m and widths of 0.2-0.5 m, reflecting the intense compaction, as observed by Qin Zhang et al. (2020) using SEM images (Figure 19A) [99]. When the pore size was calculated using the equivalent area circle method, it was discovered that the pores in clay minerals typically have a diameter between 10.25 and 419.68 nm, with an average of 43.03 nm. Although the carbonate is easily dissolved, it has little impact on the formation of micropores. Other studies have also reported on this discovery. The average pore size of the dissolved pores in carbonate is 59.8 nm, with a range from 31.72 to 733.32 nm (Figure 19B). Shale samples have a low concentration of feldspar, which ranges from 0% to 12% on average. Feldspar is another mineral that dissolves readily; typically, larger pores develop as a result of the process. The feldspar does not dissolve, though, because of the sample's higher carbonate content (8.0%–50.6%). Feldspar has a lot of cleavage, so it has a lot of cleavage cracks. These cracks have an average diameter of 37.67 nm and a diameter range of 28.8 to 415.55 nm, according to the equivalent circle area calculation (Figure 19C). Due to this negative correlation between feldspar content and fractal dimension, an increase in feldspar causes a decrease in pore complexity and an increase in shale pore size.

DOI: 10.31695/IJASRE.2025.4.2

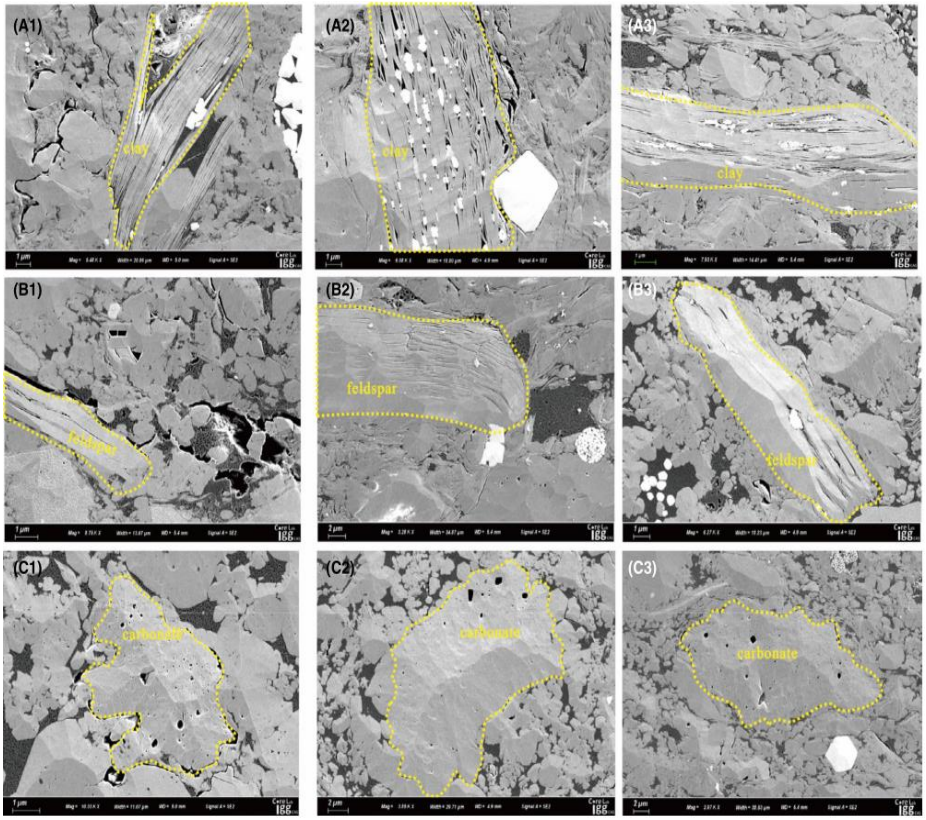

Fig.19: Pore development in (A) clay minerals, (B) feldspar, and (C) carbonate of the Longmaxi Formation, Weiyuan shale gas field. [99]

In order to discuss the effects of shale compositions on the pore structure of adsorbed pores in marine shale, Haijiao Fu et al. (2022) methodically investigated the relationships between pore structural parameters at different scales (i.e., micropore volume, micropore surface area, and average pore diameter, BET surface area, and BJH pore volume) and shale compositions (i.e., quartz, clay, and TOC) [92]. These relationships are shown in Figs. 20. The Fig. 20 shows how the TOC content affects quartz content, micropore area, BJH pore volume and micropore volume. First off, the TOC content and quartz content have a clear positive correlation (Fig. 20a). According to earlier research, this positive correlation may be connected to the quartz's biogenic source [100]. The TOC content also exhibits blatantly positive correlations with micropore volume and micropore surface area (Figs. 20b, c), suggesting that the organic matter in marine shale should primarily provide micropores (1.7 nm) in that material. Thirdly, the TOC content shows significantly positive correlations with BET surface area, but a weak correlation with BJH pore volume (Figs. 20d, 20e). The analysis indicates that surface area of the larger pores (1.7–300 nm) is also mainly provided by OM, while pore volume may be influenced by the other factors, except for OM.

DOI: 10.31695/IJASRE.2025.4.2

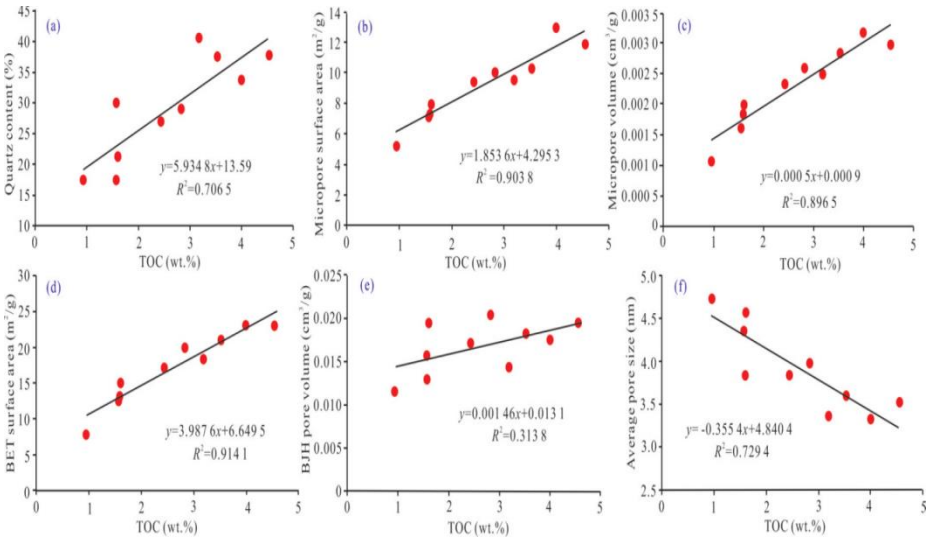

Figure 20. Relationships between the TOC content and quartz content (a), micropore surface area (b), micropore volume (c), BET surface area (d), BJH pore volume (e), and average pore diameter (f). [92]

4.2.3. Correlation between thermal maturity and pore structure

The pore structure of shale gas reservoirs and thermal maturity have a complex relationship. Shale pores associated with organic matter and clay minerals form during hydrocarbon generation and thermal evaluation [34, 101]. For instance, the immature stage of organic matter is nonporous, whereas the mature stage has an increase in the volume and number of organic pores. As thermal maturity increases, mesopores and micropores develop into macropores. Thermal maturation, on the other hand, reduces total pore volume and specific surface area, which could result in pore collapse and reduced pore development in the overmatured stage [102]. For instance, as organic matter is buried deeper and compacted, its thermal evaluation rises, causing pore blockage and a reduction in the development of pore networks. High thermal maturity also alters the type and weight of clay minerals, as well as the surface area and pore volume, reducing the pore structure parameters. Based on the correlation between pore structure and thermal maturity, several studies have identified specific ranges. For instance, according to Wei et al. (2018)), thermal maturity ranges between 0.7% and 3.5% and enhances pore development [103].

Six samples of Longmaxi shale from wells YS118 and JY2 in the Sichuan Basin were examined by Guang Hu et al. (2020) using ion beam-environmental scanning electron microscopy (FIB-SEM) and low-pressure N^2 adsorption and desorption [31]. They discovered that thermal maturity, macerals, and palynomorphs have a significant impact on the development of organic pores. The findings indicate that sample YS-01's OM surface porosity (Requ = 2.70%) is lower than sample JY-01's (Requ = 2.48%), and that the volume of organic pores decreases with increasing maturity. Pressure coefficient and compaction, in addition to thermal maturity, can also influence the development and characteristics of organic pores [104, 105]. According to Y.X. Liu et al. (2017), when the OM is in the high and over-mature stage, its porosity is higher at higher pressure [106]. Well JY2 has a lower pressure coefficient than well YS118 (P.W. Wang et al., 2018) [107]. It is anticipated that sample YS- 01 from well YS118 will have a higher surface porosity of OM than sample JY-01 from well JY2. According to earlier research, the volume of organic pores increases with maturity before decreasing with high and over-maturity [108, 109]. The critical maturity level at which an increase in organic-pore volume changes to a decrease is uncertain, though. According to several studies the critical value of maturity is 2.5% Ro [110].

Tonglou Guo et al. (2023) investigated the impact of thermal maturity on pore structure characteristics in typical shale samples (Fig.21) [94]. TOC content was used to normalize the micropore volume and specific

DOI: 10.31695/IJASRE.2025.4.2

surface area in order to prevent the influence of TOC content. Among the analyzed samples, the shale with the highest median Ro (S741) had the greatest micropore volume and specific surface area. Pang et al. (2019) discovered that the organic porosity of shales in the southern Sichuan Basin rose at first and subsequently reduced as thermal maturity increased (Fig.21a) [111]. In the same location, a comparable relationship has been observed between shale porosity and thermal maturity.

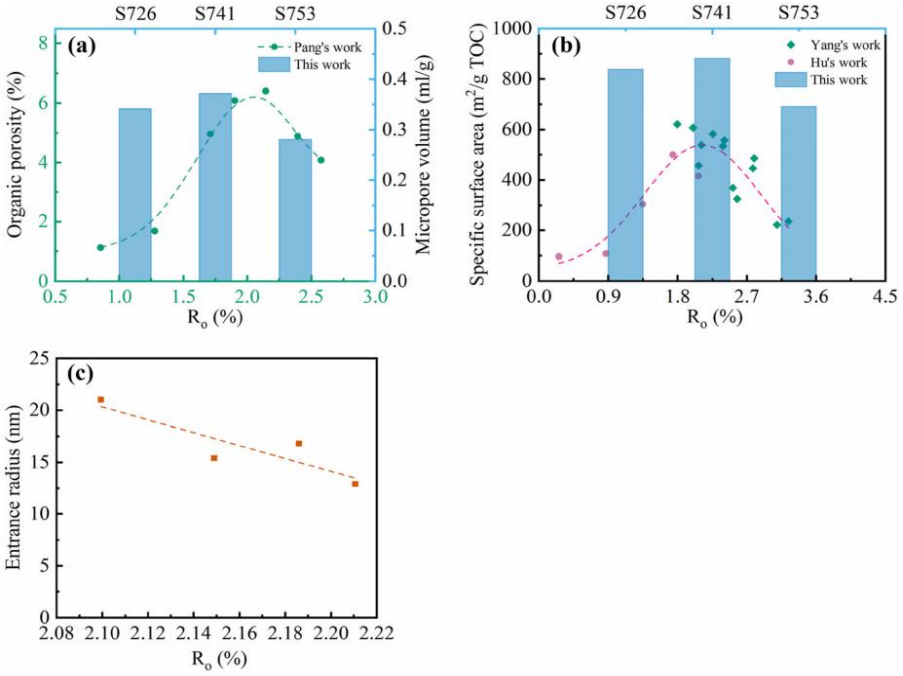

Fig.21: Effect of thermal maturity (Ro) of the shale samples on their: (a) micropore volume; (b) specific surface area; (c) entrance radius. [94]

As the organic matter progressed from the immature to the over-mature stage, the findings of Hu et al. (2015) revealed a maximum TOC-normalized specific surface area at Ro of about 2.0% (Fig. 21b) [112]. According to Loucks et al. (2009), hydrocarbon generation is linked to the increase in micropore volume and specific surface area in the early thermal maturation stage, which increases the quantity and size of micropores in shale's organic matter [82]. The carbonization of organic matter, which is typically linked to the collapse and fusion of organic pores, can be blamed for the declining trend of micropore volume and specific surface area at the over-mature stage. Additionally, mechanical compaction caused by burial depth can cause pores to reorganize, particularly in cases where those pores are not shielded by rigid mineral frameworks. According to Fig. 21c, the burial depth grows as thermal maturity rises, and the entrance radius of shales can decrease as mechanical compaction rises (Fig. 21c).

4.3. Rock-fluid reaction in the fracturing, production, and storage.

At higher temperatures, the fluid-rock contact results in an exchange of elements or isotopes. Diffusion, chemical exchange processes, redox reactions, dissolution-precipitation, and their mixtures are all included in the interaction. Oil and gas extraction from low permeability shale reservoirs has increased significantly as a result of the development and application of hydraulic fracturing techniques [113, 114]. Significant amounts of fracturing fluids are injected into underground shale formations during hydraulic fracturing operations, but only 1% to 30% of the fluids could be recovered [115]. These leftover hydraulic fracturing fluids (HFF) in the reservoirs may trigger a variety of processes, including cation exchange and redox of solid and aqueous components, claim. Such reactions may lead to the dissolution and precipitation of minerals, alter the permeability and mechanical integrity of the reservoirs, and impact the effectiveness of oil and gas production and water recovery [116, 117]. Since the industry is aware that hydraulic fracturing

DOI: 10.31695/IJASRE.2025.4.2

fluids have the potential to harm well productivity, numerous chemicals are added to HHF to lessen reservoir damage [118]. Recent studies, however, have revealed that these additives are occasionally ineffective at stopping the alteration of common minerals (such as clay minerals, calcite, and barite) [119]. The shut-in period, which occurs days to months after hydraulic fracturing but before well production, is the most likely time period for the shale property change related to HFF. It is debatable whether these interactions occur on a timescale relevant to the rock soaking in the HHF because it is unclear how much the chemical interactions between shales and these introduced fluids alter fluid and rock properties during this time. Therefore, experimental research is required to assess the potential contribution of fluid-rock interaction to the alteration of shale mineral composition and porosity and to better understand the reactions that are likely to occur upon exposure of shales to HHF. Though the interaction of common mineral with HHF have been well investigated and documented in the lab, these investigations are usually done in isolation with an emphasis on a particular reaction (e.g., calcite dissolution or barite precipitation) [120, 121].

The mineral behaviors and pore structures of the Silurian Longmaxi formation were examined by Ganlin Hua et al. (2021) using X-ray diffraction (XRD), a field emission scanning electron microscope (FE-SEM), QEMSCAN, computed tomography (CT) scanning, nitrogen adsorption testing, and organic geochemical analysis [122]. They came to the conclusion that while the fracturing fluid and deionized water did not noticeably alter organic matter, they did have a variety of effects on carbonate minerals. Quartz, albites, and illites remained largely unaltered, but calcites and dolomites were significantly dissolved. In the deionized water-shale interaction, dolomites crystals precipitated more frequently than in the fracturing fluid-shale interaction, and some fractures appeared to be filled with flocculated friction reducers or deposited mineral particles. The fracturing fluid could increase pore connectivity and volume, and after 120 hours, the depth of the fluid invasion was about 60 m. When compared to the initial sample, the calculated 3D pore volume increased by 67% at 24 hours, 117% at 72 hours, and 430% at 120 hours as a result of the dissolved pores and loosening/shedding of particles that were detected by CT over time.

4.3.1. Effects of fracturing fluid on Longmaxi shale formation

According to Ganlin Hua et al (2021), after being exposed to the fracturing fluid, carbonate minerals disintegrated and continuously created new space as the experiments were running [123]. Some carbonate minerals, particularly calcite, disintegrated and created dissolved pores and mottled surfaces on the sample (Fig. 22(A)–(D)). Compared to calcite, dolomite underwent a more subtle change that involved secondary pores (1 m) along the boundary and micro-fractures inside the particles (Fig. 22(A)-(D)). Albite and quartz, two brittle minerals, were essentially insoluble in the fracturing fluid (Fig. 22(A)-(D)). Illite in particular, a clay mineral, seemed to be relatively stable, with barely perceptible changes (Fig. 22(E) and (F)). The initial sample contained organic pores that were present and roughly ranged in size from 0.01 m to 0.3 m (Fig. 22(E) and (F)). The organic matter was comparatively stable and showed no obvious changes after the FFSI experiment (Fig. 22(E) and (F)).

DOI: 10.31695/IJASRE.2025.4.2

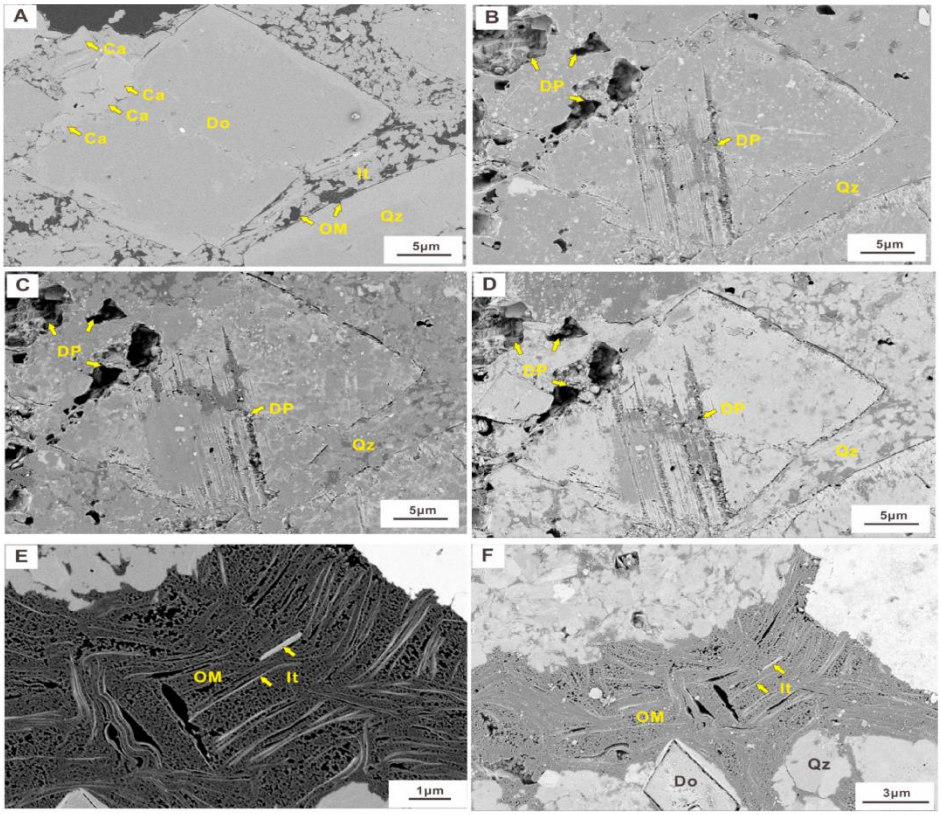

Fig. 22. SEM photos of mineral and pore changes before and after the FFSI, Sample A. (Ca-Calcite, Do-Dolomite, Qz-Quartz, It-Illite, OM-Organic matter, DP- Dissolution pores). (A) Initial sample, and some pores were observed in the calcite, organic matter and dolomite; (B) Sample after 24 h' reaction, calcites were dissolved and removed totally. In addition, some dissolution pores were developed inner the dolomite and its boundary; (C) Sample after 72 h' reaction, and the enlargement of the dissolution pores was observed; (D) Sample after 120 h' reaction. (E) Initial sample, and OM pores and illites were observed; (F) Sample after 120 h' reaction, and no obvious changes were observed in OM pores and illites. [123]

The XRD (Fig.23) results of Qiao Lyu et al (2020) revealed that the shale sample composition changed noticeably when it came into contact with both the fracturing fluid and deionized water [124]. For example, clay minerals changed minimally after being treated with the fracturing fluid, but brittle minerals such as quartz, albite, and carbonate minerals changed dramatically, particularly the carbonate minerals (calcite and dolomite) (Fig.23). Calcite concentration was initially 26.7%, but dropped to 19.8% after 120 hours of interaction with fracturing fluid. Dolomite also declined from 13.2% to 9.7%. Quartz, on the other hand, jumped from 39.9% to 47.9%. The initial albite content was low (3%) and stayed constant (3.2%). In contrast to the considerable shift in carbonate minerals, the fracturing fluid generated only a little change in clay minerals, increasing iolite and chlorite from 11.3% to 14.8% and 0.4% and 1.3%, respectively.

DOI: 10.31695/IJASRE.2025.4.2

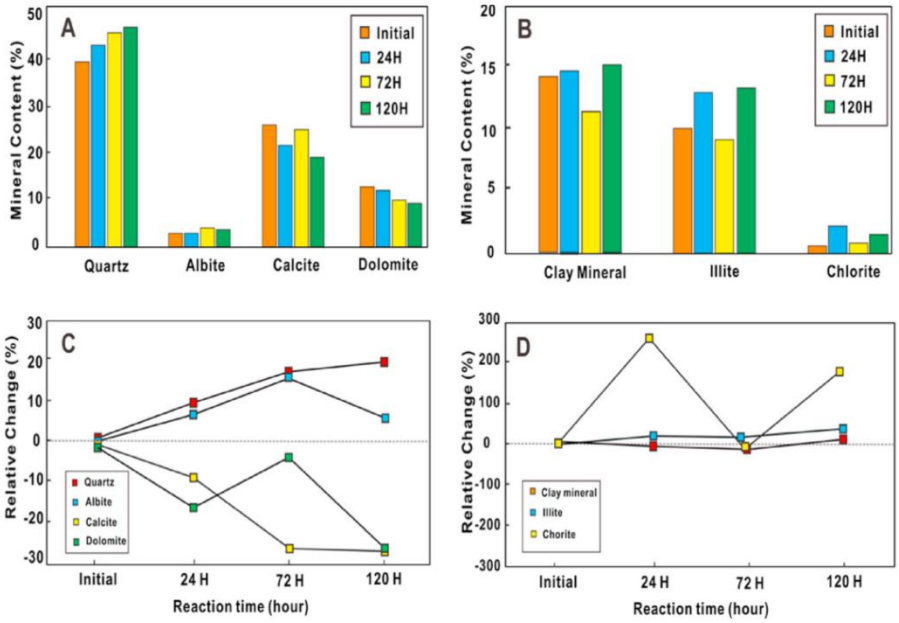

Fig. 23. Mineralogy changes during different stages of FFSI experiment, Sample A. (A) Non-clay mineral content; (B) Clay minerals content; (C) Relative change rate of non-clay minerals; (D) Relative change rate of clay minerals. [124]

Under real subsurface circumstances, the development of minerals and pores in organic-rich marine shales differed substantially. Carbonate minerals seemed to be considerably dissolved, according to XRD and SEM data [125, 126]. The tests of Ganlin Hua et al (2021) revealed that the dissolution and deposition of various minerals, such as quartz, albite, and illite, were indistinguishable [122]. Carbonate mineral dissolution was shown to improve the porosity and connectedness of the sample. The position of the new pores may be determined from the original mineral distribution in the sample. Isolated calcite grains were present in the sample at first, but fell off following contact with the fracturing fluid, resulting in distinct voids.

Also, Qiao Lyu et al (2020) reviewed some papers about fluid-rock interactions in hydraulic fracturing and noticed that, For SC-CO_2 fracturing, most of the injected CO_2 also stays in the reservoirs [124]. As the production of one shale gas well will last several years or decades, the fluids in the reservoirs have sufficient time to penetrate shale's pores, cracks and fractures, and fluid-rock reactions occur during the gas recovery process. Chemical and physical reactions are among the reactions. Swelling or shrinkage are physical reactions, and mineral dissolution or precipitation are chemical reactions. The two types of reactions interact with one another. While the chemical reactions for various fracturing techniques vary, the physical reactions in gas and liquid fracturing are comparable and are brought on by adsorption.

For liquids like water or brine, the possible reactions are as follows [127, 128]:

$$Ca(Mg, Fe)\,CO_3 + 2H^+ \leftrightarrow Ca^{2+} + 0.5Mg^{2+} + 0.5Fe^{2+} + 2HCO_3^-$$

$$4FeS_2 + 14O_2 + 4H_2O \leftrightarrow 4Fe^{2+} + 8(SO_4)^{2-} + 8H^+$$

$$2Fe^{3+} + 3H_2O \leftrightarrow Fe_2O_3 + 6H^+$$

For gases like CO_2 , the possible reactions are as follows [129]:

$$CO_2 + H_2O \leftrightarrow H_2CO_3 \leftrightarrow H^+ + HCO_3^- \leftrightarrow 2H^+ + CO_3^{2-}$$

$$KAlSi_3O_8 + 2H^+ + H_2O \leftrightarrow 2K^+ + Al_2Si_2O_5(OH)_4 + 4SiO_2$$

$$NaAlSi_3O_8 + CO_2 + H_2O \leftrightarrow NaAlCO_3(OH)_2 + 3SiO_2$$

DOI: 10.31695/IJASRE.2025.4.2

$CaCO_3 + H^+ \leftrightarrow Ca^+ + HCO_3^-$

$Ca(OH)_2 + CO_2 \leftrightarrow CaCO_3 + H_2O$

$Fe^{2+} + HCO_3^- \leftrightarrow FeCO_3 + H^+$

$Fe^{2+} + Mg^{2+} + Ca^{2+} + 3HCO_3^- \leftrightarrow CaFeMg(CO_3)_3 + 3H^+$

The mineral compositions of shale rocks are directly tied to the chemical processes. The chemical reactions are more intense when the fracturing fluid is a combination, such as foam including water and CO_2 [130]. This is due to the low pH of CO_2-dissolved water, which is less than 3 when CO_2 is in the supercritical phase [131].

4.3.2. Main controlling factors on the fluid-shale interaction

The effects of FFSI on reservoir characteristics during "well shut-in after fracturing" are difficult to predict because it is influenced by numerous factors, both internal and external, over the course of a few days and involves physical and chemical interactions between fluids and reservoirs under high temperature and high pressure [132]. Temperature, pressure, experimental time, and fracturing fluid formulation are examples of external factors that have typically been taken into account as experimental parameters in earlier studies. Researchers typically set up average values of these two parameters, or install them as normal pressure and temperature, and focus on the influence of experimental time and different fluids because of the specific regional variations in temperature and pressure [133, 134].

Porosity will typically increase and fractures will widen as the experimental period is extended [135]. Additionally, shale swelling and induced porosity alternations tend to produce different phenomena with different additives in different solutions, such as natural spring water and reused processed water [136]. The mineral compositions and pore structures of reservoirs are the main internal factors. Previous studies have found that shale mineralogy can affect porosity and permeability by producing new pores in acidic environments and changing the pore structure which showed that, compared to the dissolution of feldspathic minerals (albite) and silicate minerals (quartz), the dissolution of carbonate minerals (calcite and dolomite) was rapid [137, 138]. Additionally, dolomite and calcite disintegrated differently [139]. This analysis suggests that the carbonate mineral contents of shale, particularly calcite, dissolve more readily and result in greater porosity when reacting with fracturing fluid at high temperatures and pressure.

4.3.3. Shale Gas occurrence types

Different formation physics and pore properties influence the types of natural gas in shale formations. Free gas, adsorbed gas, and dissolved gas are three potential states of underground gas occurrence according to the classification of pore structures in shale formations. Free gas is typically kept in pore systems, including both organic and inorganic pores, in addition to fractures [140]. Gas storage and seepage mechanisms differ significantly across pore sizes [141]. Most adsorbate gas is kept in equilibrium with free gas on the surface of organic matter. Dissolved gas is typically kept in formation water, liquid hydrocarbons, but most importantly, solid kerogen. Shale gas is continuously produced by organic kerogen, which also acts as the source rock [142]. The percentage of various gas types varies from reservoir to reservoir because pressure, temperature, organic matter types, content, and maturity, the emergence of microfractures, and liquid hydrocarbon content all have a significant impact. Figure 24 illustrates the various gas types and gas flow mechanisms in organic shale nanopores.

DOI: 10.31695/IJASRE.2025.4.2

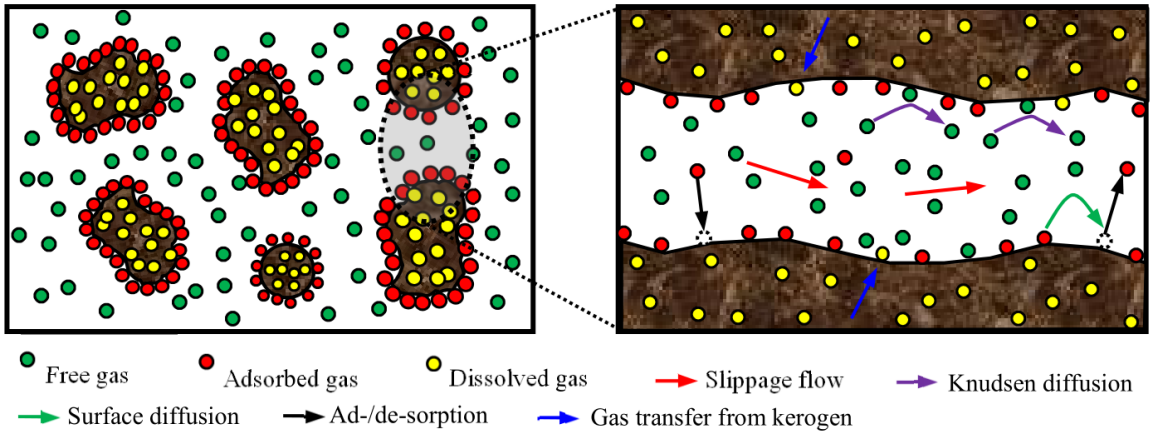

Fig.24: The storage form and flow mechanism of shale gas in organic nanopores [142]

By thoroughly utilizing core observation, thin-section analysis, SEM analysis, and emission scanning electron microscopy after argon ion polishing technologies, they developed a new classification method of gas storage space in shale formations based on earlier studies [143, 144]. In actuality, free gas is kept in pores, microfractures, and hydraulic fractures, whether they are organic or inorganic. Adsorbed gas and dissolved gas work together to determine the amount of free gas. A free gas state only exists when the total amount of gas is greater than the sum of the adsorbed and dissolved gas amounts. The ideal gas equation of state (EOS) is not satisfied by gas behaviors in high-pressure or high-temperature reservoir conditions, so the real gas EOS must be used to describe these behaviors [145, 146]. Also, adsorbed gas can make up 20–85% of all gas reserves and is primarily stored on the surface of matrix particles, kerogen, and clay minerals [147]. Physical adsorption includes gas adsorption on shale matrix particles. Although adsorbed gas is a part of the overall gas production, its precise percentage is unclear. The percentage of adsorbed gas in original gas in place (OGIP) is much clearer when compared to its contribution to total gas production. According to recent research, adsorbed gas makes up between 30 and 50% of OGIP when the pressure is higher than 13.79 MPa and between 50 and 80% when the pressure is lower [148, 149].

When the maturity of organic matter is greater than 0.6%, organic nanopores with a size range of 5-750 nm are significantly developed in shale gas reservoirs [150]. Organic matter has a large surface area because the pores have a small radius. For instance, in nanoporous kerogen, the specific surface area can reach 300 m^2/g [151]. The vast surface area offers locations that are ideal for gas adsorption. Pore structures, mineral compositions, the degree of metamorphism, gas constituents, pressure, temperature, water vapor content, etc. are the main factors affecting the gas adsorption capacity. Since organic matter is the primary storage type for adsorbed gas, the TOC content has a sizable impact on the amount of adsorbed gas in shale gas reservoirs.

The adsorbed gas content and TOC content in various shale gas reservoirs have a positive correlation, as shown in Figure 25. This is due to the fact that a high TOC content indicates that there is more organic matter in the shale matrix, which, due to its substantial surface area, can offer enough room for gas storage. Using the Barnett Shale as an example, Figure 25 illustrates how we can identify various gas types based on how much gas is adsorbed and how much total gas is present in the shale matrix. While the amount of free gas in the inorganic matrix is unaffected by the TOC content, both adsorbed gas and free gas in the organic matrix increase as the TOC content rises. Adsorption and desorption of gas are significant factors to consider when estimating reserves of shale gas in shale gas plays [18, 152]. If we investigate the situation further, we might wonder how much adsorbed gas might be created during the extraction of shale gas and how much gas adsorption and desorption impact gas transient flow patterns in shale gas reservoirs.

DOI: 10.31695/IJASRE.2025.4.2

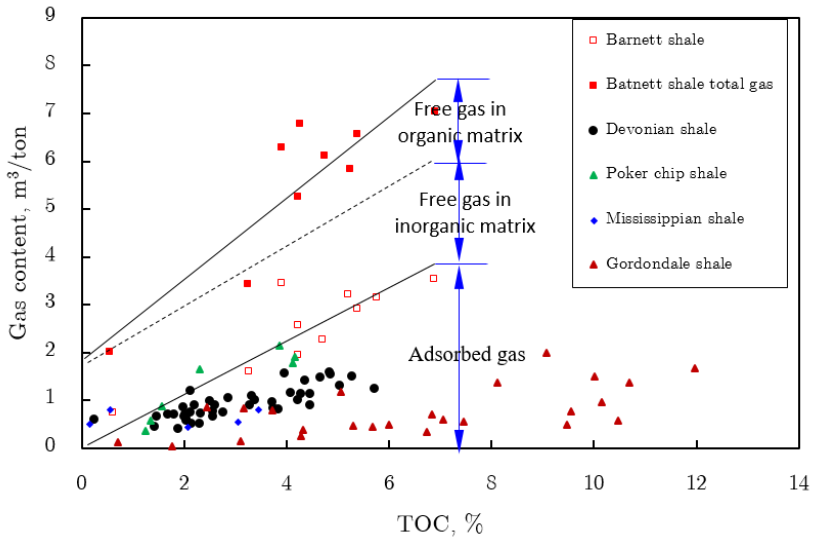

Fig.25: Adsorbed gas in different shales and its relationship with TOC content (revised from [153]

5. SUMMARY

The design and optimization of hydraulic fracturing—which is required for production from shale gas reservoirs with a present recovery rate of less than 20%—is greatly influenced by the geomechanical properties acquired from the use of various experimental methodologies. The use of various experimental techniques has demonstrated that stress, pressure, temperature, bedding plane orientation, fluid saturation, gas adsorption, and shale mineralogy have a significant impact on how shale geomechanical properties behave under various testing conditions (drained/undrained and loading/unloading). Shale is difficult to coring, retrieve, handle, and preserve for geomechanical testing due to its brittleness, diverse mineralogical composition, low porosity, ultra-low permeability, and sensitivity to contacting fluid. Fracture propagation can be predicted more precisely by knowing the connections between a shale formation's geomechanical characteristics and its stress condition. This is necessary for effective planning and execution. In general, experimental methods for shale geomechanical evaluation include uniaxial and triaxial compression, Ultrasonic testing, and nano-indentation. The most appropriate experimental technique is ultrasound testing because it has the potential to increase the accuracy of the results of geomechanical evaluation. All other experimental methods permanently harm shale samples that are not readily accessible.

The relationship between the Longmaxi Shale formation's geochemical, mineralogical composition, and geomechanical characteristics has been reviewed in this work, and the probable brittleness and fractability of the potential unconventional reservoir have been highlighted. Quartz (SiO2) makes up the majority of the inorganic part of the Longmaxi Shale as determined by XRD and XRF studies. Calcite (CaO) is the main mineral found in carbonates. Illite and kaolinite are the major clay minerals, with muscovite being found in trace amounts. The set of results of the studies carried out in the Longmaxi shale formation, had shown that rock compositions exert a first-order control on brittleness, in particular clay minerals, which result in decreased brittleness and increases ductility. The mineral makeup of the rock samples has a significant impact on the geomechanical properties of the Longmaxi Shale as applied. One of the key elements influencing how a shale formation reacts to hydraulic fracture stimulation is its geomechanical characteristics. It was determined that the Longmaxi Shale's shale mineralogy was the primary influence on these features. While Poisson's ratio rises relative to clay mineral increase and causes ductility of the shale to rise as well, Young's modulus and brittleness typically increase as clay minerals decrease and/or as silica (quartz) with carbonate (calcite) concentration increases. The association between the quartz content and the TOC (total organic content) is positive while the correlation between the quartz and clay is negative. The shale matrix's reservoir space is mostly made up of inter-crystal micropores and organic matter pores. The porosity and TOC volume are found to be positively correlated. Shale velocities are dependent on the

DOI: 10.31695/IJASRE.2025.4.2

confining pressure, and the patterns of velocity fluctuation show how the various shale pore types affect the velocities.Due to the variance in load-bearing grains from clay to quartz, the influence of quartz on P-wave velocity impedances exhibits a distinctive V-shape trend, whilst the influence of quartz on the Vp/Vs ratio exhibits a single declining trend. In both shale formations, the total pore volume and specific surface area are positively linked with the TOC, siderite, and quartz minerals, indicating that the pore system is controlled by both organic and inorganic fabrics. The difference in specific surface areas of clay types as detected in image analysis may explain why Illite contributes more to the growth of pores than kaolinite, according to the association of clay types with total pore volume and specific surface area. The development of pores is strongly influenced by the thermal maturity; as Ro% grew during a thermal evaluation, the number of organic and inorganic pores (micropores and mesopores) in the investigated shale formations increased. With an increase in burial depth, the proportion of macropores first rose and then fell, and the trend of micropores was the opposite of that of mesopores. The percentage of macropores had a strong positive correlation with TOC content, a weak positive correlation with the percentage of micropores, and a negative correlation with the percentage of mesopores. In the deep shale under study, the percentage of producible porosity (average 11.81%) was only moderate; as burial depth increased, it first increased and then decreased. The ratio of producible porosity was strongly positively correlated with both the proportion of macropores and the TOC content. This suggests that organic matter controlled the development of macropores, which in turn controlled the connectivity of the pores in the deep shale under study.

DECLARATION OF COMPETING INTEREST

The authors declare that there is no conflict of interest.

DATA AVAILABILITY

No data was used for the research described in the article.

REFERENCES

1. Ross, D.J. and R.M. Bustin, Shale gas potential of the lower Jurassic Gordondale member, northeastern British Columbia, Canada. Bulletin of Canadian petroleum geology, 2007. **55**(1): p. 51-75.
2. Montgomery, M.H., A new technique for probing convection in pulsating white dwarf stars. The Astrophysical Journal, 2005. **633**(2): p. 1142.
3. Qun, L., et al., Progress and prospects of horizontal well fracturing technology for shale oil and gas reservoirs. Petroleum Exploration and Development, 2022. **49**(1): p. 191-199.
4. Kim, J. and G.J. Moridis, Numerical analysis of fracture propagation during hydraulic fracturing operations in shale gas systems. International Journal of Rock Mechanics and Mining Sciences, 2015. **76**: p. 127-137.
5. Tuzingila, R.M., L. Kong, and R. Koy Kasongo, A review on experimental techniques and their applications in the effects of mineral content on geomechanical properties of reservoir shale rock. Rock Mechanics Bulletin, 2024. **3**: p. 100110.
6. Zou, C., et al., Geological characteristics and resource potential of shale gas in China. Petroleum exploration and development, 2010. **37**(6): p. 641-653.
7. Ulm, F.-J. and Y. Abousleiman, The nanogranular nature of shale. Acta Geotechnica, 2006. **1**: p. 77-88.
8. Bobko, C. and F.-J. Ulm, The nano-mechanical morphology of shale. Mechanics of Materials, 2008. **40**(4-5): p. 318-337.
9. Deirieh, A., et al., Nanochemomechanical assessment of shale: a coupled WDS-indentation analysis. Acta Geotechnica, 2012. **7**: p. 271-295.
10. Alstadt, K.N., K.S. Katti, and D.R. Katti, Nanoscale morphology of kerogen and in situ nanomechanical properties of green river oil shale. Journal of Nanomechanics and Micromechanics, 2016. **6**(1): p. 04015003.
11. Abedi, S., et al., Nanochemo-mechanical signature of organic-rich shales: a coupled indentation–EDX analysis. Acta Geotechnica, 2016. **11**: p. 559-572.
12. Dubey, R., et al., Can big data and predictive analytics improve social and environmental sustainability? Technological forecasting and social change, 2019. **144**: p. 534-545.
13. Kong, A., et al., The nature of nurture: Effects of parental genotypes. Science, 2018. **359**(6374): p. 424-428.
14. Liu, K. and M. Ostadhassan, Multi-scale fractal analysis of pores in shale rocks. Journal of Applied Geophysics, 2017. **140**: p. 1-10.

DOI: 10.31695/IJASRE.2025.4.2

15. Veytskin, Y.B., et al., Micromechanical characterization of shales through nanoindentation and energy dispersive x-ray spectrometry. Geomechanics for Energy and the Environment, 2017. **9**: p. 21-35.
16. Cooles, G., A. Mackenzie, and T. Quigley, Calculation of petroleum masses generated and expelled from source rocks. Organic geochemistry, 1986. **10**(1-3): p. 235-245.
17. Jarvie, D.M., Factors affecting Rock-Eval derived kinetic parameters. Chemical Geology, 1991. **93**(1-2): p. 79-99.
18. Zhang, B., et al., Review of formation and gas characteristics in shale gas reservoirs. Energies, 2020. **13**(20): p. 5427.
19. Wang, R., et al., Differential characteristics of the Upper Ordovician-Lower Silurian Wufeng-Longmaxi shale reservoir and its implications for exploration and development of shale gas in/around the Sichuan Basin. Acta Geologica Sinica-English Edition, 2019. **93**(3): p. 520-535.
20. Nie, H., Z. Jin, and R. Bian, The "source-cap hydrocarbon-controlling" enrichment of shale gas in Upper Ordovician Wufeng Formation-Lower Silurian Longmaxi Formation of Sichuan Basin and its periphery. Acta Petrolei Sinica, 2016. **37**(5): p. 557.
21. Liu, S., et al., Characteristics of the shale gas reservoir rocks in the Lower Silurian Longmaxi Formation, East Sichuan basin, China. Energy Exploration & Exploitation, 2013. **31**(2): p. 187-219.
22. Liang, C., et al., Tumor metastasis inhibition by imaging-guided photothermal therapy with single-walled carbon nanotubes. Advanced materials (Deerfield Beach, Fla.), 2014. **26**(32): p. 5646-5652.
23. Wu, Z., et al., Effect of organic matter type and maturity on organic matter pore formation of transitional facies shales: A case study on upper Permian Longtan and Dalong shales in middle Yangtze region, China. Journal of Earth Science, 2020. **31**: p. 368-384.
24. Mei, M. and B. Katz, Petroleum geochemistry, in Geochemistry and Mineral Resources. 2022, Intechopen.
25. Zhong, Y., et al., The bidirectional role of the JAK2/STAT3 signaling pathway and related mechanisms in cerebral ischemia-reperfusion injury. Experimental neurology, 2021. **341**: p. 113690.
26. Chen, S., et al., Reservoir evaluation of the Lower Silurian Longmaxi Formation shale gas in the southern Sichuan Basin of China. Marine and Petroleum Geology, 2014. **57**: p. 619-630.
27. Curiale, J.A. and J.B. Curtis, Organic geochemical applications to the exploration for source-rock reservoirs–A review. Journal of Unconventional Oil and Gas Resources, 2016. **13**: p. 1-31.
28. Hunt, S.D. and R.M. Morgan, The resource-advantage theory of competition: dynamics, path dependencies, and evolutionary dimensions. Journal of marketing, 1996. **60**(4): p. 107-114.
29. Jarvie, D.M., et al., Unconventional shale-gas systems: The Mississippian Barnett Shale of north-central Texas as one model for thermogenic shale-gas assessment. AAPG bulletin, 2007. **91**(4): p. 475-499.
30. Jinliang, G., et al., Pyrolysis of coal measure source rocks at highly to over mature stage and its geological implications. Petroleum Exploration and Development, 2020. **47**(4): p. 773-780.
31. Hu, G., et al., Seismic fault interpretation using deep learning-based semantic segmentation method. IEEE Geoscience and Remote Sensing Letters, 2020. **19**: p. 1-5.
32. Worden, R., et al., Chlorite in sandstones. Earth-Science Reviews, 2020. **204**: p. 103105.
33. Basu, S., A. Jones, and P. Mahzari, Best practices for shale core handling: transportation, sampling and storage for conduction of analyses. Journal of Marine Science and Engineering, 2020. **8**(2): p. 136.
34. Jiang, Z., et al., Basic characteristics and evaluation of shale oil reservoirs. Petroleum Research, 2016. **1**(2): p. 149-163.
35. Sayers, C., Seismic anisotropy of shales. Geophysical prospecting, 2005. **53**(5): p. 667-676.
36. Charlton, P.H., et al., Wearable photoplethysmography for cardiovascular monitoring. Proceedings of the IEEE, 2022. **110**(3): p. 355-381.
37. Charlton, P.H., et al., The 2023 wearable photoplethysmography roadmap. Physiological measurement, 2023. **44**(11): p. 111001.
38. Dandekar, P., A. Goel, and D.T. Lee, Biased assimilation, homophily, and the dynamics of polarization. Proceedings of the National Academy of Sciences, 2013. **110**(15): p. 5791-5796.
39. Fjaer, E., et al., Petroleum related rock mechanics. Vol. 53. 2008: Elsevier.
40. Zoback, M., et al., Lithosphere stress and deformation. Treatise on geophysics, 2007: p. 253-273.

DOI: 10.31695/IJASRE.2025.4.2

41. Domnesteanu, P., C. McCann, and J. Sothcott, Velocity anisotropy and attenuation of shale in under-and overpressured conditions. Geophysical Prospecting, 2002. **50**(5): p. 487-503.
42. Slatt, R.M. and Y. Abousleiman, Merging sequence stratigraphy and geomechanics for unconventional gas shales. The Leading Edge, 2011. **30**(3): p. 274-282.
43. Sone, H. and M.D. Zoback, Mechanical properties of shale-gas reservoir rocks—Part 1: Static and dynamic elastic properties and anisotropy. Geophysics, 2013. **78**(5): p. D381-D392.
44. Sayers, C., The elastic anisotrophy of shales. Journal of Geophysical Research: Solid Earth, 1994. **99**(B1): p. 767-774.
45. Zheng, D., et al., Study of anisotropic strength properties of shale. AGH Drilling, Oil, Gas, 2019. **36**(1): p. 93-112.
46. Vernik, L. and J. Milovac, Rock physics of organic shales. The leading edge, 2011. **30**(3): p. 318-323.
47. Aadnoy, B.S. and R. Looyeh, Petroleum rock mechanics: drilling operations and well design. 2019: Gulf professional publishing.
48. Anderson, T.W., Estimating linear restrictions on regression coefficients for multivariate normal distributions. The Annals of Mathematical Statistics, 1951: p. 327-351.
49. Jaeger, J., Friction of rocks and stability of rock slopes. Geotechnique, 1971. **21**(2): p. 97-134.
50. Ostadhassan, M., Geomechanics and elastic anisotropy of the Bakken Formation, Williston Basin. 2013: The University of North Dakota.
51. Ostadhassan, M., et al. Stress analysis and wellbore stability in unconventional reservoirs. in ARMA US Rock Mechanics/Geomechanics Symposium. 2013. ARMA.
52. Rasouli, A., et al., Occurrence of organic matter-rich deposits (Middle Jurassic to Lower Cretaceous) from Qalikuh locality, Zagros Basin, South–West of Iran: A possible oil shale resource. International Journal of Coal Geology, 2015. **143**: p. 34-42.
53. Iferobia, C.C. and M. Ahmad, A review on the experimental techniques and applications in the geomechanical evaluation of shale gas reservoirs. Journal of Natural Gas Science and Engineering, 2020. **74**: p. 103090.
54. Thiercelin, M.J. and R.A. Plumb, Core-based prediction of lithologic stress contrasts in East Texas formations. SPE Formation Evaluation, 1994. **9**(04): p. 251-258.
55. Tiab, D. and E.C. Donaldson, Wettability. Petrophysics, 2012. **3**: p. 371-418.
56. Nygård, R., et al., Brittle–ductile transition, shear failure and leakage in shales and mudrocks. Marine and Petroleum Geology, 2006. **23**(2): p. 201-212.
57. Ismael, M., et al., Synthesis of phase pure hexagonal YFeO3 perovskite as efficient visible light active photocatalyst. Catalysts, 2017. **7**(11): p. 326.
58. Benz, T. and R. Schwab, A quantitative comparison of six rock failure criteria. International Journal of Rock Mechanics and Mining Sciences, 2008. **45**(7): p. 1176-1186.
59. Mehranpour, M.H. and P.H. Kulatilake, Comparison of six major intact rock failure criteria using a particle flow approach under true-triaxial stress condition. Geomechanics and geophysics for geo-energy and geo-resources, 2016. **2**: p. 203-229.
60. Ismael, H.N., et al., The morbidity and mortality of hepaticojejunostomies for complex bile duct injuries: a multi-institutional analysis of risk factors and outcomes using NSQIP. Hpb, 2017. **19**(4): p. 352-358.
61. Donath, F.A., Experimental study of shear failure in anisotropic rocks. Geological Society of America Bulletin, 1961. **72**(6): p. 985-989.
62. Jaeger, C., Rock mechanics and engineering. 1979: Cambridge University Press.
63. Vernik, L. and M.D. Zoback, Estimation of maximum horizontal principal stress magnitude from stress-induced well bore breakouts in the Cajon Pass scientific research borehole. Journal of Geophysical Research: Solid Earth, 1992. **97**(B4): p. 5109-5119.
64. Alejano, L.R. and A. Bobet, Drucker–prager criterion, in The ISRM suggested methods for rock characterization, testing and monitoring: 2007-2014. 2014, Springer. p. 247-252.
65. Mode, A.W., et al., Geochemical and mineralogical controls on the geomechanical properties of the Eze-Aku Shale: Implications for a potential hydrocarbon reservoir. Journal of African Earth Sciences, 2022. **196**: p. 104698.

DOI: 10.31695/IJASRE.2025.4.2

66. Xian, S., et al., Investigation of mechanical properties of bedded shale by nanoindentation tests: A case study on Lower Silurian Longmaxi Formation of Youyang area in southeast Chongqing, China. Petroleum Exploration and Development, 2019. **46**(1): p. 163-172.
67. Li, H.L., et al., Damage localization, sensitivity of energy release and the catastrophe transition. Earthquake Processes: Physical Modelling, Numerical Simulation and Data Analysis Part I, 2002: p. 1933-1950.
68. Vořechovský, M. and V. Sadílek, Computational modeling of size effects in concrete specimens under uniaxial tension. International journal of fracture, 2008. **154**: p. 27-49.
69. Jia, Y., et al., Laboratory characterization of cyclic hydraulic fracturing for deep shale application in Southwest China. International Journal of Rock Mechanics and Mining Sciences, 2021. **148**: p. 104945.
70. Tuzingila, R.M., L. Kong, and R.K. Kasongo, Experimental Techniques and Rock Physics Modeling to Study the Effects of Mineral Content and Thermal Maturation on Elastic Properties of the Organic-Rich Shale: Case Study of the Longmaxi Formation. SPE Journal, 2025: p. 1-22.
71. Gao, W., et al., The status, challenges, and future of additive manufacturing in engineering. Computer-aided design, 2015. **69**: p. 65-89.
72. Jia, Y., et al., Laboratory geomechanical and petrophysical characterization of Longmaxi shale properties in Lower Silurian Formation, China. Marine and Petroleum Geology, 2021. **124**: p. 104800.
73. Lu, Y., et al., A study of variation in the initiation pressure and fracture distribution patterns of raw coal in SC-CO2 fracturing under the true tri-axial system. Rock Mechanics and Rock Engineering, 2022. **55**(6): p. 3425-3438.
74. Xu, H., et al., Effects of concentration of sodium hypochlorite as an endodontic irrigant on the mechanical and structural properties of root dentine: A laboratory study. International endodontic journal, 2022. **55**(10): p. 1091-1102.
75. Meng, M., et al., Fractal characterization of pore structure and its influence on salt ion diffusion behavior in marine shale reservoirs. International Journal of Hydrogen Energy, 2020. **45**(53): p. 28520-28530.
76. Yin, J., et al., Large increase in global storm runoff extremes driven by climate and anthropogenic changes. Nature communications, 2018. **9**(1): p. 4389.
77. Chai, B., et al., Lithofacies Types and Reservoir Characteristics of Mountain Shale in Wufeng Formation-Member 1 of Longmaxi Formation in the Complex Structural Area of Northern Yunnan–Guizhou. ACS omega, 2023. **8**(2): p. 2085-2097.
78. Fan, C., et al., Geological conditions and exploration potential of shale gas reservoir in Wufeng and Longmaxi Formation of southeastern Sichuan Basin, China. Journal of Petroleum Science and Engineering, 2020. **191**: p. 107138.
79. Yonghong, F., et al., Microscopic pore-fracture configuration and gas-filled mechanism of shale reservoirs in the western Chongqing area, Sichuan Basin, China. Petroleum Exploration and Development, 2021. **48**(5): p. 1063-1076.
80. Guo, X., et al., Characteristics and controlling factors of micropore structures of the Longmaxi Shale in the Jiaoshiba area, Sichuan Basin. Natural Gas Industry B, 2014. **1**(2): p. 165-171.
81. Liu, Z., et al., Types and quantitative characterization of microfractures in the continental shale of the Da'anzhai member of the Ziliujing Formation in Northeast Sichuan, China. Minerals, 2021. **11**(8): p. 870.
82. Loucks, R.G., et al., Morphology, genesis, and distribution of nanometer-scale pores in siliceous mudstones of the Mississippian Barnett Shale. Journal of sedimentary research, 2009. **79**(12): p. 848-861.
83. Rouquerol, J., et al., Recommendations for the characterization of porous solids (Technical Report). Pure and applied chemistry, 1994. **66**(8): p. 1739-1758.
84. Sun, W., et al., Pore characteristics and evolution mechanism of shale in a complex tectonic area: Case study of the Lower Cambrian Niutitang Formation in Northern Guizhou, Southwest China. Journal of Petroleum Science and Engineering, 2020. **193**: p. 107373.
85. Li, X., et al., Influence of pore structure particularity and pore water on the occurrence of deep shale gas: Wufeng–Longmaxi formation, Luzhou block, Sichuan basin. Natural Resources Research, 2022. **31**(3): p. 1403-1423.
86. Yang, R., et al., Spontaneous imbibition of three leading shale formations in the Middle Yangtze Platform, South China. Energy & Fuels, 2017. **31**(7): p. 6903-6916.

DOI: 10.31695/IJASRE.2025.4.2

87. Löhr, S., et al., Is organic pore development in gas shales influenced by the primary porosity and structure of thermally immature organic matter? Organic Geochemistry, 2015. **87**: p. 119-132.
88. Mayer, L.M., Relationships between mineral surfaces and organic carbon concentrations in soils and sediments. Chemical Geology, 1994. **114**(3-4): p. 347-363.
89. Zhao, L., W. Zheng, and X. Cao, Distribution and evolution of organic matter phases during biochar formation and their importance in carbon loss and pore structure. Chemical engineering journal, 2014. **250**: p. 240-247.
90. Ma, L., et al., Multi-scale 3D characterisation of porosity and organic matter in shales with variable TOC content and thermal maturity: Examples from the Lublin and Baltic Basins, Poland and Lithuania. International Journal of Coal Geology, 2017. **180**: p. 100-112.
91. Deng, J., et al., Dynamic elastic properties of the Wufeng–Longmaxi formation shale in the southeast margin of the Sichuan Basin. Journal of Geophysics and Engineering, 2014. **11**(3): p. 035004.
92. Fu, H., et al., Biodegradation of early thermogenic gas and generation of secondary microbial gas in the Tieliekedong region of the northern Tarim Basin, NW China. International Journal of Coal Geology, 2022. **261**: p. 104075.
93. Ross, D.J. and R.M. Bustin, The importance of shale composition and pore structure upon gas storage potential of shale gas reservoirs. Marine and petroleum Geology, 2009. **26**(6): p. 916-927.
94. Guo, T., et al., Characteristics and governing factors of pore structure and methane sorption in deep-marine shales: A case study of the wufeng–longmaxi formations, weirong shale gas field, sichuan basin. Natural Resources Research, 2023. **32**(4): p. 1733-1759.
95. Wilson, M. and L. Wilson, Clay mineralogy and shale instability: an alternative conceptual analysis. Clay Minerals, 2014. **49**(2): p. 127-145.
96. Wu, L.M., et al., Towards an understanding of the role of clay minerals in crude oil formation, migration and accumulation. Earth-Science Reviews, 2012. **115**(4): p. 373-386.
97. Mondol, N.H., et al., Experimental mechanical compaction of clay mineral aggregates—Changes in physical properties of mudstones during burial. Marine and petroleum geology, 2007. **24**(5): p. 289-311.
98. Rieke, H.H. and G.V. Chilingarian, Compaction of argillaceous sediments. Vol. 16. 1974: Elsevier.
99. Gao, F., et al., Multi-class fruit-on-plant detection for apple in SNAP system using Faster R-CNN. Computers and Electronics in Agriculture, 2020. **176**: p. 105634.
100. Yang, R., et al., Nano-scale pore structure and fractal dimension of organic-rich Wufeng-Longmaxi shale from Jiaoshiba area, Sichuan Basin: Investigations using FE-SEM, gas adsorption and helium pycnometry. Marine and Petroleum Geology, 2016. **70**: p. 27-45.
101. Tang, L., et al., Pore structure and fractal characteristics of distinct thermally mature shales. Energy & Fuels, 2019. **33**(6): p. 5116-5128.
102. Guan, M., et al., The evolution of pore structure heterogeneity during thermal maturation in lacustrine shale pyrolysis. Journal of Analytical and Applied Pyrolysis, 2022. **163**: p. 105501.
103. Wei, W., et al., Metal-Free C (sp2)–H/N–H cross-dehydrogenative coupling of quinoxalinones with aliphatic amines under visible-light photoredox catalysis. Organic Letters, 2018. **20**(22): p. 7125-7130.
104. Song, L., et al., Porosity and storage capacity of Middle Devonian shale: A function of thermal maturity, total organic carbon, and clay content. Fuel, 2019. **241**: p. 1036-1044.
105. Liu, B., et al., Impact of thermal maturity on the diagenesis and porosity of lacustrine oil-prone shales: Insights from natural shale samples with thermal maturation in the oil generation window. International Journal of Coal Geology, 2022. **261**: p. 104079.
106. Liu, Y.-X., Y. Lin, and Y. Zhou, 2D cellular automaton simulation of hot deformation behavior in a Ni-based superalloy under varying thermal-mechanical conditions. Materials Science and Engineering: A, 2017. **691**: p. 88-99.
107. Pang, Q., et al., Variation of Organic Pore Structure With Maceral Types in the Longmaxi Shale, Sichuan Basin. Front. Advances in the Exploration and Development of Unconventional Oil and Gas: From the Integration of Geology and Engineering, 2022. **9**: p. 72964423.
108. Milliken, K.L., et al., Organic matter–hosted pore system, Marcellus formation (Devonian), Pennsylvania. AAPG bulletin, 2013. **97**(2): p. 177-200.

DOI: 10.31695/IJASRE.2025.4.2

109. Modica, C.J. and S.G. Lapierre, Estimation of kerogen porosity in source rocks as a function of thermal transformation: Example from the Mowry Shale in the Powder River Basin of Wyoming. AAPG bulletin, 2012. **96**(1): p. 87-108.
110. Wang, P., et al., Pore structure characterization for the Longmaxi and Niutitang shales in the Upper Yangtze Platform, South China: Evidence from focused ion beam–He ion microscopy, nano-computerized tomography and gas adsorption analysis. Marine and Petroleum Geology, 2016. **77**: p. 1323-1337.
111. Pang, Z., et al., Antibiotic resistance in Pseudomonas aeruginosa: mechanisms and alternative therapeutic strategies. Biotechnology advances, 2019. **37**(1): p. 177-192.
112. Hu, B., et al., GSDS 2.0: an upgraded gene feature visualization server. Bioinformatics, 2015. **31**(8): p. 1296-1297.
113. Wenrui, H., W. Yi, and B. Jingwei, Development of the theory and technology for low permeability reservoirs in China. Petroleum Exploration and Development, 2018. **45**(4): p. 685-697.
114. Arthur, J.D., et al. Evaluating the environmental implications of hydraulic fracturing in shale gas reservoirs. in SPE Health, Safety, Security, Environment, & Social Responsibility Conference-North America. 2009. SPE.
115. Middleton, R.S., et al., Shale gas and non-aqueous fracturing fluids: Opportunities and challenges for supercritical CO2. Applied Energy, 2015. **147**: p. 500-509.
116. Kaszuba, J., B. Yardley, and M. Andreani, Experimental perspectives of mineral dissolution and precipitation due to carbon dioxide-water-rock interactions. Reviews in Mineralogy and Geochemistry, 2013. **77**(1): p. 153-188.
117. Cui, G., et al., Geochemical reactions and their influence on petrophysical properties of ultra-low permeability oil reservoirs during water and CO2 flooding. Journal of Petroleum Science and Engineering, 2021. **203**: p. 108672.
118. Kreipl, M. and A. Kreipl, Hydraulic fracturing fluids and their environmental impact: then, today, and tomorrow. Environmental Earth Sciences, 2017. **76**(4): p. 160.
119. Graham, G.M. and D.M. Frigo, Inorganic mineral scale mitigation, in Flow Assurance. 2022, Elsevier. p. 287-442.
120. Greenlee, L.F., et al., The effect of antiscalant addition on calcium carbonate precipitation for a simplified synthetic brackish water reverse osmosis concentrate. Water research, 2010. **44**(9): p. 2957-2969.
121. He, C. and R.D. Vidic, Impact of antiscalants on the fate of barite in the unconventional gas wells. Environmental Engineering Science, 2016. **33**(10): p. 745-752.
122. Hua, G., et al., Rock physical and chemical alterations during the in-situ interaction between fracturing fluid and Silurian organic-rich shales in China. Journal of Natural Gas Science and Engineering, 2021. **94**: p. 104075.
123. Guan, M., et al., Paleoenvironment and chemostratigraphy heterogenity of the Cretaceous organic-rich shales. Advances in Geo-Energy Research, 2021. **5**(4): p. 444-455.
124. Lyu, Q., J. Shi, and R.P. Gamage, Effects of testing method, lithology and fluid-rock interactions on shale permeability: A review of laboratory measurements. Journal of Natural Gas Science and Engineering, 2020. **78**: p. 103302.
125. Mathia, E.J., et al., Evolution of porosity and pore types in organic-rich, calcareous, Lower Toarcian Posidonia Shale. Marine and Petroleum Geology, 2016. **75**: p. 117-139.
126. Akintola, G.O., An integrated approach of determining shale gas potentiality of carbonaceous shale of the Permian Tuli Basin, Limpopo Province of South Africa. 2022.
127. Harrison, A.L., et al., Element release and reaction-induced porosity alteration during shale-hydraulic fracturing fluid interactions. Applied Geochemistry, 2017. **82**: p. 47-62.
128. Pearce, B.K., et al., Constraining the time interval for the origin of life on Earth. Astrobiology, 2018. **18**(3): p. 343-364.
129. Gaus, I., Role and impact of CO2–rock interactions during CO2 storage in sedimentary rocks. International journal of greenhouse gas control, 2010. **4**(1): p. 73-89.
130. Wanniarachchi, W., P. Ranjith, and M. Perera, Shale gas fracturing using foam-based fracturing fluid: a review. Environmental Earth Sciences, 2017. **76**: p. 1-15.

DOI: 10.31695/IJASRE.2025.4.2

131. Toews, K.L., et al., pH-defining equilibrium between water and supercritical CO2. Influence on SFE of organics and metal chelates. Analytical Chemistry, 1995. **67**(22): p. 4040-4043.
132. Perera, M., A review of underground hydrogen storage in depleted gas reservoirs: Insights into various rock-fluid interaction mechanisms and their impact on the process integrity. Fuel, 2023. **334**: p. 126677.
133. Mallepally, R.R., et al., Fluid properties at high pressures and temperatures: Experimental and modelling challenges. The Journal of Supercritical Fluids, 2018. **134**: p. 33-40.
134. Bradshaw, P., Experimental Fluid Mechanics: The Commonwealth and International Library: Thermodynamics and Fluid Mechanics Division. 2016: Elsevier.
135. Nelson, R.A. An experimental study of fracture permeability in porous rock. in ARMA US Rock Mechanics/Geomechanics Symposium. 1976. ARMA.
136. Gholami, R., et al., A review on borehole instability in active shale formations: Interactions, mechanisms and inhibitors. Earth-Science Reviews, 2018. **177**: p. 2-13.
137. Wu, W. and M.M. Sharma. Acid fracturing shales: effect of dilute acid on properties and pore structure of shale. in SPE Hydraulic Fracturing Technology Conference and Exhibition. 2015. SPE.
138. Bustin, R.M., et al. Impact of shale properties on pore structure and storage characteristics. in SPE shale gas production conference. 2008. SPE.
139. Chakhmouradian, A.R., E.P. Reguir, and A.N. Zaitsev, Calcite and dolomite in intrusive carbonatites. I. Textural variations. Mineralogy and Petrology, 2016. **110**: p. 333-360.
140. Cai, J., et al. Ntire 2019 challenge on real image super-resolution: Methods and results. in Proceedings of the IEEE/CVF Conference on Computer Vision and Pattern Recognition Workshops. 2019.
141. Liehui, Z., et al., Review of micro seepage mechanisms in shale gas reservoirs. International Journal of Heat and Mass Transfer, 2019. **139**: p. 144-179.
142. Javadpour, F., CO2 injection in geological formations: determining macroscale coefficients from pore scale processes. Transport in porous media, 2009. **79**(1): p. 87-105.
143. Curtis, M.E. Structural characterization of gas shales on the micro-and nano-scales. in SPE Canada Unconventional Resources Conference? 2010. SPE.
144. Ju, Y., et al., Three-dimensional characterisation of multi-scale structures of the Silurian Longmaxi shale using focused ion beam-scanning electron microscopy and reconstruction technology. Journal of Natural Gas Science and Engineering, 2017. **46**: p. 26-37.
145. Guo, P., et al., The determination of phase behavior properties of high-temperature high-pressure and rich condensate gases. Fuel, 2020. **280**: p. 118568.
146. Varzandeh, F., E.H. Stenby, and W. Yan, General approach to characterizing reservoir fluids for EoS models using a large PVT database. Fluid Phase Equilibria, 2017. **433**: p. 97-111.
147. Thomas, K.M., Perspectives of gas adsorption and storage in kerogens and shales. Energy & Fuels, 2023. **37**(4): p. 2569-2585.
148. Mahmoud, M., Effect of gas adsorption on the estimation of gas in place (GIP) in conventional and unconventional reservoirs. Arabian Journal for Science and Engineering, 2019. **44**: p. 6205-6214.
149. Abolghasemi, E., Influence of Adsorption Layer Thickness in Tight Compressible Shales subject to Gas Production. 2020.
150. Wei, M., et al., Main factors influencing the development of nanopores in over-mature, organic-rich shales. International Journal of Coal Geology, 2019. **212**: p. 103233.
151. Taotao, C., et al., Characteristics of organic pores in Middle and Upper Permian shale in the Lower Yangtze region. Petroleum Experimental Geology, 2018. **40**(3): p. 315-322.
152. Yang, Y. and S. Liu, Review of shale gas sorption and its models. Energy & Fuels, 2020. **34**(12): p. 15502-15524.
153. Wang, F.P., et al. Pore networks and fluid flow in gas shales. in SPE Annual Technical Conference and Exhibition? 2009. SPE.

DOI: 10.31695/IJASRE.2025.4.2